Icarus 250 (2015) 602–622

Contents lists available at ScienceDirect

Icarus

journal homepage: www.elsevier.com/locate/icarus

Extent, age, and resurfacing history of the northern smooth plains on Mercury from MESSENGER observations

Lillian R. Ostrach [a,b,*], Mark S. Robinson [a], Jennifer L. Whitten [c,d], Caleb I. Fassett [e], Robert G. Strom [f], James W. Head [c], Sean C. Solomon [g,h]

[a] School of Earth and Space Exploration, Arizona State University, Tempe, AZ 85287, USA
[b] NASA Goddard Space Flight Center, Greenbelt, MD 20771, USA
[c] Department of Earth, Environmental and Planetary Sciences, Brown University, Providence, RI 02912, USA
[d] Center for Earth and Planetary Studies, Smithsonian Institution, Washington, DC 20004, USA
[e] Department of Astronomy, Mount Holyoke College, South Hadley, MA 01075, USA
[f] Lunar and Planetary Laboratory, University of Arizona, Tucson, AZ 85721, USA
[g] Department of Terrestrial Magnetism, Carnegie Institution of Washington, Washington, DC 20015, USA
[h] Lamont-Doherty Earth Observatory, Columbia University, Palisades, NY 10964, USA

ARTICLE INFO

Article history:
Received 22 August 2014
Revised 4 November 2014
Accepted 7 November 2014
Available online 17 November 2014

Keywords:
Mercury
Mercury, surface
Volcanism
Cratering

ABSTRACT

MESSENGER orbital images show that the north polar region of Mercury contains smooth plains that occupy ~7% of the planetary surface area. Within the northern smooth plains (NSP) we identify two crater populations, those superposed on the NSP ("post-plains") and those partially or entirely embayed ("buried"). The existence of the second of these populations is clear evidence for volcanic resurfacing. The post-plains crater population reveals that the NSP do not exhibit statistically distinguishable subunits on the basis of crater size–frequency distributions, nor do measures of the areal density of impact craters reveal volcanically resurfaced regions within the NSP. These results suggest that the most recent outpouring of volcanic material resurfaced the majority of the region, and that this volcanic flooding emplaced the NSP over a relatively short interval of geologic time, perhaps 100 My or less. Stratigraphic embayment relationships within the buried crater population, including partial crater flooding and the presence of smaller embayed craters within the filled interiors of larger craters and basins, indicate that a minimum of two episodes of volcanic resurfacing occurred. From the inferred rim heights of embayed craters, we estimate the NSP to be regionally 0.7–1.8 km thick, with a minimum volume of volcanic material of 4×10^6 to 10^7 km^3. Because of the uncertainty in the impact flux at Mercury, the absolute model age of the post-plains volcanism could be either ~3.7 or ~2.5 Ga, depending on the chronology applied.

1. Introduction

The MErcury Surface, Space ENvironment, GEochemistry, and Ranging (MESSENGER) spacecraft (Solomon et al., 2001), inserted into orbit around Mercury on 18 March 2011, acquired images that enabled systematic mapping of the planet's north polar region (50–90°N) for the first time. Earlier Mariner 10 and MESSENGER flyby image coverage (e.g., Murray et al., 1974a; Danielson et al., 1975; Trask and Guest, 1975; Solomon et al., 2008) of Mercury's north polar region at illumination and viewing geometries favorable for morphological studies was limited, but such images showed large regions of smooth plains surrounded by more heavily cratered terrain (e.g., Danielson et al., 1975; Trask and Guest, 1975; Grolier and Boyce, 1984; Robinson et al., 1999; Solomon et al., 2008). Mercury Dual Imaging System (MDIS) (Hawkins et al., 2007) images of the north polar region acquired from orbit provide full coverage at resolutions higher than those attained previously, at low emission angle and at illumination favorable for morphological assessment.

Two major terrain units dominate the north polar region: the northern heavily cratered terrain (NHCT) and the northern smooth plains (NSP). Heavily cratered regions of Mercury are superposed by numerous impact craters that are closely packed and often overlapping (Murray et al., 1974b; Trask and Guest, 1975; Gault et al., 1977; Fassett et al., 2011). An intercrater plains unit was mapped by Trask and Guest (1975) and was described as gently rolling ground between and around large craters of the heavily cratered terrain. The difference between the intercrater plains and

* Corresponding author at: NASA Goddard Space Flight Center, 8800 Greenbelt Rd., Code 698, Greenbelt, MD 20771, USA.
E-mail address: lillian.r.ostrach@nasa.gov (L.R. Ostrach).

http://dx.doi.org/10.1016/j.icarus.2014.11.010
0019-1035/

heavily cratered terrain is complex; obvious superposition relations were not commonly observed in Mariner 10 images (e.g., Trask and Guest, 1975; Malin, 1976; Leake, 1982; Whitten et al., 2014). As a result and because of the difficulty of separating these two units, the intercrater plains and heavily cratered terrain were frequently combined into a single unit, e.g., for determining the size–frequency distribution of impact craters (Strom et al., 1975a; Trask, 1975; Guest and Gault, 1976), and we follow that practice in this study.

The northern smooth plains are relatively flat, have fewer superposed impact craters than the surrounding heavily cratered terrain (Murray et al., 1974b; Strom et al., 1975b; Guest and Gault, 1976), and are morphologically similar to the lunar maria (e.g., Murray et al., 1974a, 1974b; Murray, 1975; Strom et al., 1975b; Head et al., 2008, 2011). Smooth plains units identified from Mariner 10 images (e.g., Murray et al., 1974b; Murray, 1975) have a lower crater density than the heavily cratered terrain, indicating that the smooth plains are resolvably younger. Although no diagnostic volcanic features or constructs were conclusively identified in the Mariner 10 images, possibly due to resolution and illumination limitations (Schultz, 1977; Malin, 1978; Milkovich et al., 2002), a volcanic origin for much of the smooth plains was favored on the basis of their widespread distribution, embayment relations with surrounding topography, visible color properties, relatively young age, and superposed tectonic features (e.g., Murray et al., 1974b; Strom et al., 1975b; Trask and Strom, 1976; Kiefer and Murray, 1987; Spudis and Guest, 1988; Robinson and Lucey, 1997; Robinson and Taylor, 2001). Although a volcanic origin for smooth plains on Mercury was called into question (Wilhelms, 1976; Oberbeck et al., 1977), and although it is certainly possible that some smooth plains deposits are impact-generated products (i.e., fluidized ejecta, impact melt), most regions of smooth plains are now interpreted as products of effusive volcanism, much like the lunar maria (Murray et al., 1974b; Murray, 1975; Trask and Guest, 1975; Strom et al., 1975b; Trask and Strom, 1976; Kiefer and Murray, 1987; Robinson and Lucey, 1997; Head et al., 2008, 2009a, 2011; Murchie et al., 2008; Robinson et al., 2008; Solomon et al., 2008; Denevi et al., 2009, 2013a; Ernst et al., 2010; Fassett et al., 2009; Kerber et al., 2009, 2011; Watters et al., 2009, 2012; Prockter et al., 2010; Freed et al., 2012; Klimczak et al., 2012; Byrne et al., 2013; Hurwitz et al., 2013; Goudge et al., 2014).

The extent and influence of volcanism over geologic time on Mercury may be inferred from the impact cratering record of volcanically resurfaced regions, partial flooding of crater floors, regional plains formation, and large-scale burial of pre-existing terrain (e.g., Head et al., 2009a, 2009b). This study examines the local stratigraphy of the north polar region, complementing previous studies of other regions with smooth plains units (Trask, 1975; Strom, 1977; Spudis and Guest, 1988; Strom and Neukum, 1988; Strom et al., 2008, 2011; Fassett et al., 2009; Head et al., 2011; Denevi et al., 2013a). We also place the units in the north polar region into the context of Mercury's global stratigraphic record. The results presented here add to our understanding of the volcanic history of Mercury by comparing the relative ages of the NSP and the Caloris smooth plains (Spudis and Guest, 1988; Strom and Neukum, 1988; Strom et al., 2008; Fassett et al., 2009; Head et al., 2011; Denevi et al., 2013a) as well as the relative ages of the NSP and the surrounding NHCT. Moreover, the heavily cratered terrain in the north polar region is compared with heavily cratered terrain elsewhere on Mercury (e.g., Strom et al., 2008, 2011; Fassett et al., 2011). The relative timing of NSP emplacement is explored with crater size–frequency distributions, measures of the areal density of craters, and stratigraphic relations. The results of this assessment provide evidence for multiple resurfacing events within the NSP over a short geologic interval. We also present regional estimates of NSP thickness and volume derived from embayed craters, thereby providing a minimum estimate of the amount of volcanic material contained within this occurrence of smooth plains.

2. Methods and data

We first constructed a monochrome mosaic in polar stereographic projection from 50°N to 90°N and spanning all longitudes at a resolution of 400 m per pixel from MDIS wide-angle camera (WAC) images (749 nm wavelength, Hawkins et al., 2007; Fig. 1a). Individual MDIS WAC observations with images centered between 50°N and 90°N were selected and processed with the Integrated Software for Imagers and Spectrometers (ISIS) package provided by the U.S. Geological Survey. As a result of geospatial referencing, the corners of images centered at 50°N at times extend southward to ~43–46°N, and geologic units and their surface areas were determined from this original mosaic; figures of the north polar region in this paper are nonetheless masked south of 50°N for clarity.

On the basis of morphological observations, two distinct geologic units, NHCT and NSP, were defined in the north polar region, over a total surface area of 9.26×10^6 km^2 (Fig. 1b). The NHCT occupies 3.67×10^6 km^2 of the polar region (~40% of the study area and ~5% of the surface area of Mercury). Impact crater morphologies in the NHCT range from pristine with visible ejecta ray systems and sharp rim crests (morphological Class 1) to barely discernable and highly degraded craters (morphological Class 4 or 5) (Arthur et al., 1964). Primary craters identified in the NHCT are as large as ~350 km in diameter, and there is a profusion of secondary craters intermingled with the primaries.

There are two large areas of smooth plains within the north polar region that together occupy a total area of 5.59×10^6 km^2 (~60% of the study area and ~7% of the surface area of Mercury). The larger region of smooth plains (NSP1 in Fig. 1b) is 4.08×10^6 km^2 in area and extends beyond our study region to ~40°N between ~40°E and 80°E (Head et al., 2011). Within NSP1 is a region of smooth plains occupying 2.92×10^5 km^2 described but not included in the continuous NSP by Head et al. (2011). The smaller region, NSP2 (Fig. 1b), extends from ~50°N to 65°N and ~120°E to 220°E and is 1.51×10^6 km^2 in area. NSP1 is connected to NSP2 by flooded craters and a series of broad valleys filled with smooth plains interpreted as volcanically flooded impact-sculpted terrain (Byrne et al., 2013; Hurwitz et al., 2013). The smaller region of smooth plains (NSP2) has contributions of material from both the inferred lava channels and the Caloris exterior smooth plains (Denevi et al., 2013a).

2.1. Crater size–frequency distributions

We measured impact craters to determine their size–frequency distribution (SFD) in areas of interest with the CraterTools extension (Kneissl et al., 2011) for the ESRI ArcMap 10 geographic information system program. The CraterTools extension computes a best-fit circle to three user-defined points on a crater rim and records the central latitude, longitude, and diameter to a project database. Primary impact craters were identified on the basis of having nearly to entirely continuous rims with approximately circular shapes. Obvious secondary craters, identified by their occurrence in chains, herringbone patterns, or clustered groups, were excluded. Secondary craters become an important contributor to the crater population at larger diameters on Mercury than on the Moon; a distinct upturn with decreasing diameter in the relative SFD plot – often termed an R plot (Crater Analysis Techniques Working Group, 1979) – at diameters near 8–10 km and smaller is interpreted as the result of including these larger secondaries

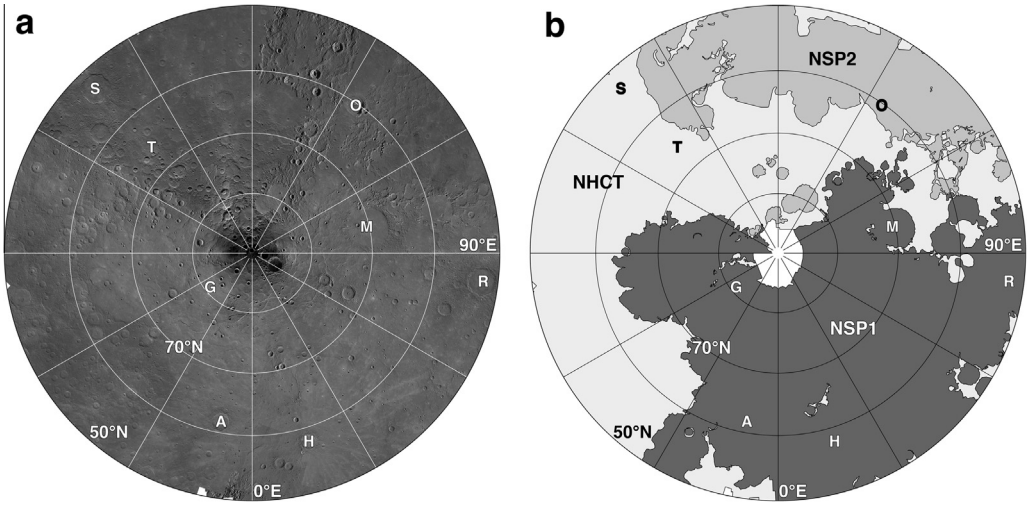

Fig. 1. Northern hemisphere of Mercury. (a) MESSENGER MDIS WAC orbital monochrome mosaic of the north polar region (400 m per pixel). The mosaic extends from 50°N to 90°N. Eight impact craters are identified with capital letters: A, Abedin, centered at 61.76°N, 349.35°E, diameter (D) = 116 km; G, Goethe (81.50°N, 306.17°E, D = 317 km); H, Hokusai (57.75°N, 16.90°E, D = 114 km); O, Oskison (60.38°N, 145.36°E, D = 122 km); M, Mendelssohn (70.07°N, 102.55°E, D = 291 km); R, Rustaveli (52.55°N, 82.59°E, D = 200 km); S, Strindberg (53.21°N, 223.44°E, D = 189 km); T, Turgenev (65.63°N, 223.64°E, D = 136 km). (b) Sketch map of geologic units in the north polar region: NSP1 (dark gray) and NSP2 (light gray) comprise the NSP; NHCT is the northern heavily cratered terrain. Selected craters are marked as in (a). A region at the pole was excluded from mapping because the determination of stratigraphic relations was rendered difficult by the oblique lighting conditions. Polar stereographic projection.

(e.g., Gault et al., 1975; Trask, 1975; Strom, 1977; Strom et al., 2008, 2011). Despite the presence of primary craters with diameters <8–10 km on the NSP, we restricted the craters in the populations used for the SFDs and for relative and absolute model age determination to those with diameter $\geqslant$8 km to limit the influence of secondary craters on our analysis.

Two plotting techniques were used to analyze crater SFDs. We generated both cumulative SFD plots and R plots to characterize crater populations, following standard root-2 binning (Crater Analysis Techniques Working Group, 1979). Standard deviation in a given bin was estimated from the square root of the number of craters in the bin. We also calculated the cumulative number of craters, $N(D)$, equal to or larger than a given diameter D per unit area (usually 10^6 km^2; e.g., Neukum, 1983), where D is expressed in kilometers. This measure of relative crater frequency allows quantitative comparison of crater populations across different studies and provides a means to determine relative ages of different geologic units.

2.2. Mapping buried craters

Two crater populations are observed in the NSP (Head et al., 2011): superposed primary impact craters ("post-plains craters") and partially to fully embayed impact craters ("buried craters"). Completely buried craters were mapped by identifying arcuate wrinkle ridges that are thought to have nucleated above, and so demarcate, buried crater rims (Watters, 1993; Klimczak et al., 2012; Watters et al., 2012), and partially buried craters were mapped when $\leqslant$25% of the crater rim was exposed. Identification of buried craters is difficult, because these impact structures are more susceptible to complete removal from the observed cratering record by emplacement of the plains, as well as by formation of post-plains craters and associated ejecta deposits. As a result, the buried crater measurement area is limited to a subsection of NSP1, comprising an area of 3.79×10^6 km^2, to exclude NSP modified by the Rustaveli impact ("R" in Fig. 1). The NSP2 region was excluded from mapping because of modification by recent impacts, including Oskison crater ("O" in Fig. 1), and poor illumination conditions for discerning buried craters. To maintain consistency with measurements of the NHCT and post-plains crater populations, we included only those buried craters $\geqslant$8 km in diameter in our crater size–frequency measurements and age determination.

We adopted a conservative mapping approach to emphasize the unambiguous identification of relict, completely buried craters. Images obtained at high solar incidence angles (>65°, measured from the vertical) typically have long shadows that emphasize subtle morphological variations so that wrinkle ridges marking rims of buried craters are readily identifiable. Smaller buried craters ($\leqslant$25–30 km in diameter), however, are more difficult to discern on the basis of tectonic structures, even at high solar incidence angles, because of the widespread occurrence and complexity of wrinkle ridges and lobate scarps within the NSP (Head et al., 2011; Watters et al., 2012). Thus, the number of buried craters identified should be regarded as a minimum figure.

2.3. Estimating regional thickness and volume of smooth plains material

The thickness of the NSP was estimated from relations between crater depth and diameter determined by Pike (1988) (Table 1) and recently confirmed with MESSENGER flyby data (Barnouin et al., 2012) in a manner similar to the method used by Head et al. (2011). We measured the diameters of buried craters from visible remnants of the crater rim, if evident, and from arcuate wrinkle ridges assumed to overlie the original crater rim where no remnant of the rim survives. Pre-flooding rim height was estimated from measurements on fresh craters on Mercury (Pike, 1988), and the thickness of plains material for a fully buried crater was estimated from the minimum thickness of material needed to cover the crater rim. A range of volumes was then estimated by multiplying the rim heights for the smallest and largest fully buried craters by the area of the appropriate subsection of the NSP study region.

There are several limitations to this technique. Mathematical relationships between crater diameter and rim height were developed for craters on Mercury only for diameters between 2.4 km and 43 km because of limited coverage of larger, partially shadowed craters (Pike, 1988). Although recent work on the relation between crater depth and diameter (from 1.3 km to ~130 km in diameter; Barnouin et al., 2012) shows that earlier relationship to be valid, the Pike (1988) equations may overestimate crater

Table 1
Relation between crater rim height or depth and diameter (Pike, 1988).

Crater type[a]	Rim height		Depth to diameter	
	Diameter (km)	Equation	Diameter (km)	Equation
Simple	2.4–12	$0.052D^{0.930}$	0.2–14.4	$0.199D^{0.995}$
Immature complex	13–43[b]	$0.150D^{0.487}$	9.5–29	$0.410D^{0.490}$
Mature complex	–[c]	–	30–175	$0.353D^{0.496}$

[a] Refer to Pike (1988) for detailed descriptions of crater morphology.
[b] Extrapolated to larger diameters, per confirmation by Barnouin et al. (2012).
[c] Equation not derived by Pike (1988).

rim height because the ratio of diameter to depth tends to decrease for larger craters ($D > 30$ km), particularly at the transitions between crater morphological types (e.g., immature complex to mature complex craters; e.g., Williams and Zuber, 1998; Baker et al., 2011; Barnouin et al., 2012). Moreover, because the crater preservation state at the time of embayment is unknown, these equations likely overestimate the rim heights of degraded craters, which tend to be lower than those of pristine craters. The NHCT and post-plains crater populations contain craters with a range of degradation states, and it is likely that the buried crater population had a range of degradation states before it was buried as well. Furthermore, when a crater is completely filled and embayed, the thickness of the volcanic material above the crater rim is unknown, so crater rim heights provide only minimum estimates of the local thickness of volcanic material. Despite these uncertainties, this method has been widely employed to produce estimates of volcanic deposit thicknesses for the lunar maria (e.g., De Hon, 1974).

2.4. Areal density of craters

We applied a measure of statistical point density to determine if individual subunits with the NSP were identifiable from the post-plains crater population. Because older surfaces are expected to have accumulated more craters per area than younger surfaces, a measure of the areal density of impact craters should reflect variations in relative age and thus indicate regions of resurfacing. We used the methodology of Ostrach and Robinson (2014) that minimizes edge effects by employing a weighted edge correction. We determined the areal density of all circular craters $\geqslant$4 km in diameter for the NSP. Although some craters between 4 km and 8 km in diameter may be unrecognized secondaries, we limited the possible incorporation of secondaries by mapping only circular, non-overlapping craters in accordance with the procedure of Ostrach and Robinson (2014).

To map the areal density of craters we used a moving neighborhood approach that determines the number of craters within a defined circular region about each output cell. Varying the neighborhood radius alters the spatial structure observed in the density map; small neighborhood sizes emphasize local (possibly statistical) variations, whereas larger neighborhood sizes tend to smooth actual variations.

For this region of Mercury, we used a moving neighborhood radius of 250 km and an output cell size of 10 km to ensure that differences related to age were emphasized. For the NSP, areal density determined for $N(8)$ and a neighborhood radius of 250 km does not provide statistically robust results (e.g., >30 samples; Silverman, 1986; Davis, 2002); the number of craters per average neighborhood, n, is 18. However, n is 53 for the areal density determined for $N(4)$, and the standard deviation (estimated as $n^{0.5}$ for n craters) is 7.3, meaning that the $N(4)$ density map is robust against statistical fluctuations within the crater measurements at the ~13% level on terrain of average age. Therefore, in density maps generated from $N(4)$ measurements, most of the variation reflects statistically significant differences, which are related to resolvable differences in relative age.

Given that impact cratering is assumed to be a spatially and temporally random process (e.g., McGill, 1977), the areal density may be described by a spatially random (Poisson) point distribution (e.g., Silverman, 1986; Davis, 2002). Accordingly, Poisson probabilities can be calculated to assess the statistical significance related to neighborhood selection. When the 10th percentile is calculated for the average neighborhood with $n = 53$ craters, there is an ~9% chance that a neighborhood will contain <44 craters or an ~10% chance that the neighborhood will contain >62 craters, and only a 1% chance that a neighborhood will contain <38 craters or >76 craters. These Poisson probabilities indicate that the usage of a 250 km neighborhood radius is acceptable (that is, a statistically robust population is being sampled), and for a spatially random crater population, ~81% of the measured neighborhoods will contain between 44 and 62 craters. However, when the neighborhood radius is decreased to 100 km, $n = 9$ and there is an ~12% chance that the neighborhood will contain <6 craters or an ~7% chance that the neighborhood will contain >13 craters, indicating that most of the density variation is statistical in nature and the neighborhood area is too small. In contrast, when the neighborhood radius is increased to 500 km, $n = 214$. There is an ~10% chance that the neighborhood will contain <196 craters or >232 craters, and although the average sample size is statistically robust, determining the influence of statistical variation within the crater frequency at the regional scale will be difficult, and regional boundaries, if present, will be overly smoothed, suggesting that a 500 km radius is too large.

To establish regions where areal density values reflect geological differences rather than statistical variation, the Create Random Points tool in ArcMap 10 was used to generate synthetic density maps. This tool calculates a statistically random distribution for a user-specified number of points within a designated polygon. The number of points used was determined from the measured crater SFD for $D \geqslant 4$ km for the NSP post-plains crater population and rounded to the nearest hundred; 1500 random points were generated on the basis of the measurement of 1519 NSP post-plains craters with $D \geqslant 4$ km.

3. Crater size–frequency distributions for Mercury's north polar region

3.1. Northern heavily cratered terrain

We were unable to distinguish subunits within the NHCT with confidence on the basis of crater SFDs, morphological relations, or color properties. The color properties of the NHCT are distinct from those of the NSP in that the NHCT have a visible and near-infrared spectral reflectance that is generally less steep with increasing wavelength (i.e., "bluer") than that of the NSP (Fig. 2), and a clear color difference follows the majority of the defined morphological boundary. This relationship is consistent with those

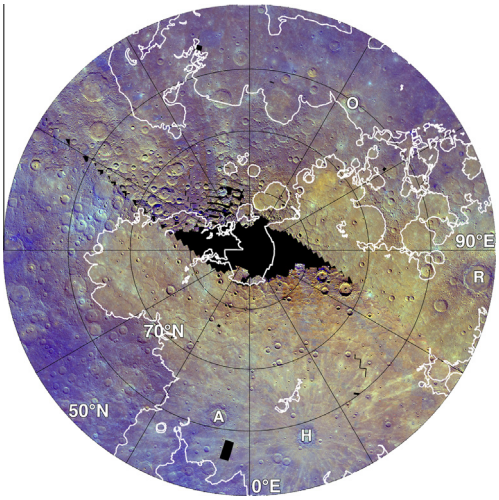

Fig. 2. MDIS WAC principal component and ratio composite (second principal component in red, first principal component in green, and the ratio of reflectance at 430 nm to that at 1000 nm in blue; Denevi et al., 2009) for the north polar region of Mercury. NHCT is bluer than the majority of NSP, which tend to be characterized by a reddish-orange color. Several impact craters are labeled: A, Abedin (61.76°N, 349.35°E), D = 116 km; H, Hokusai (57.75°N, 16.90°E), D = 114 km; O, Oskison (60.38°N, 145.36°E), D = 122 km; R, Rustaveli (52.55°N, 82.59°E), D = 200 km. Mosaic is at a resolution of 665 m per pixel and is in polar stereographic projection; black regions are gores in the color coverage.

observed between heavily cratered terrain and smooth plains mapped elsewhere on Mercury (Robinson and Lucey, 1997; Robinson and Taylor, 2001; Robinson et al., 2008; Denevi et al., 2009, 2013a). Subtle regional color variation is difficult to determine within the NHCT because the current photometric correction is limited at the large solar incidence angles that characterize images acquired at high latitudes (>60°N) (Domingue et al., 2013), and calibration artifacts for a portion of the period over which images were acquired may further complicate the determination of spectral subunits within the NHCT (Keller et al., 2013). In conjunction with the color observations, morphology observations may be used to identify stratigraphic relations at the local scale (e.g., impact crater superposition relations) within the NHCT, but any further attempt to define regional subunits is difficult.

In an effort to distinguish subunits, we divided the NHCT into three arbitrary subregions of comparable surface area, and we determined the cumulative SFDs of impact craters in each subregion. To provide robust results and minimize bias, we repeated this process twice after shifting the areal boundaries. At most crater diameters, the NHCT cumulative SFDs are statistically indistinguishable (Fig. 3) and exhibit similar slopes. At diameters $\geqslant$50 km, the cumulative frequencies of the three subregions diverge, but this outcome is likely the result of small-number statistics; within the largest-diameter bins there may be as few as one crater. The broad contiguous regions (areas 1 and 2 in Fig. 3b and c) are statistically indistinguishable from each other as well as from the cumulative SFD for the entire NHCT, but the dissected region of NHCT (area 3 in Fig. 3b and c) has an overall lower cumulative distribution. In the entire NHCT region we examined, NHCT craters are as large as ~350 km in diameter, and $N(10) = 234 \pm 8$ and $N(20) = 104 \pm 5$. (The range in these quantities for the three sets of three subregions examined is given in Appendix A, Table A1). The NHCT cumulative SFD exhibits an approximately constant slope (Fig. 4a). On an R plot, the NHCT has a relative SFD similar to that of heavily cratered terrain elsewhere on Mercury as determined by Strom et al. (2008) (Fig. 4b) and Fassett et al. (2011).

3.2. Post-plains craters in the northern smooth plains

As with the NHCT, we were unable to distinguish subunits within the NSP on the basis of the post-plains crater population. MDIS color images show that the NSP exhibit a distinct color signature from the surrounding NHCT but are internally homogeneous (Fig. 2). Variation in color within the NSP (excluding materials excavated by impact) at the regional scale is similar to the uncertainties remaining in the calibration (Domingue et al., 2013; Keller et al., 2013). No evidence for the presence of morphological or color subunits was observed in the NSP.

To search for statistically distinguishable subunits within the NSP post-plains crater population, we divided NSP1 into four subregions of similar areas in three separate iterations (Fig. 5). The NSP2 area was not included because post-plains SFD comparisons between NSP1 and NSP2 reveal that these two regions are statistically indistinguishable (Fig. 6). The absence of craters $\geqslant$100 km in diameter within NSP2 is attributed to its substantially smaller area, contributing to poor counting statistics at larger crater diameters. The cumulative SFDs for the arbitrary subregions in the NSP are statistically indistinguishable over all diameters (Fig. 5), and $N(10)$ values are nearly identical (Appendix A, Table A2). At diameters $\geqslant$40 km, the cumulative frequencies noticeably diverge because of small sample sizes.

The post-plains cumulative SFD has a lower density of craters at all diameters than the NHCT and displays a constant slope for craters in bins $\leqslant$100 km diameter (Fig. 4a). For some crater populations on volcanic units on other bodies, deflections of the observed cumulative SFD from that expected on the basis of a theoretical primary crater production function, if known, have been documented and interpreted as evidence for resurfacing (e.g., Neukum and Horn, 1976). In such settings, there can be a distinct "kink" or offset in the cumulative SFD over a given narrow range of diameters, and portions of the SFD at lesser and greater diameters correspond to different model ages (e.g., Hiesinger et al., 2002; Williams et al., 2008), enabling ages to be estimated both for the older original surface and the younger surface of the volcanic deposits. In other situations, in contrast, the complexity of resurfacing in a region may leave the crater SFD without distinct kinks (e.g., Michael and Neukum, 2010). The post-plains cumulative SFD for the NSP exhibits no evident kinks (Fig. 4a). Post-plains craters are as large as ~190 km in diameter, and within the NSP $N(10) = 63 \pm 3$ and $N(20) = 23 \pm 2$. (The range in these quantities for the three sets of four subregions examined is given in Appendix A, Table A2). These crater densities agree with those measured for the NSP post-plains population from early orbital data (with which a smaller region was investigated; Head et al., 2011) and are consistent with values for both Caloris exterior and interior smooth plains (Strom et al., 2008; Fassett et al., 2009; Denevi et al., 2013a). In the R plot, the SFD for the post-plains crater population on the NSP is statistically indistinguishable from those for the Caloris plains (Fig. 4b) (Strom et al., 2008), having a relatively flat slope and exhibiting a different shape from the SFD for the NHCT (Fig. 4b).

3.3. Buried craters

3.3.1. Morphological relations

There is abundant evidence of embayment relations between the NSP and pre-existing craters. There are remnant crater rims (Figs. 7 and 8a), partially embayed craters and basins (e.g., Goethe, Fig. 8a), and tectonic features interpreted to be the result of deformation concentrated over buried crater rims (Fig. 8; e.g., Head et al., 2011; Klimczak et al., 2012; Watters et al., 2012).

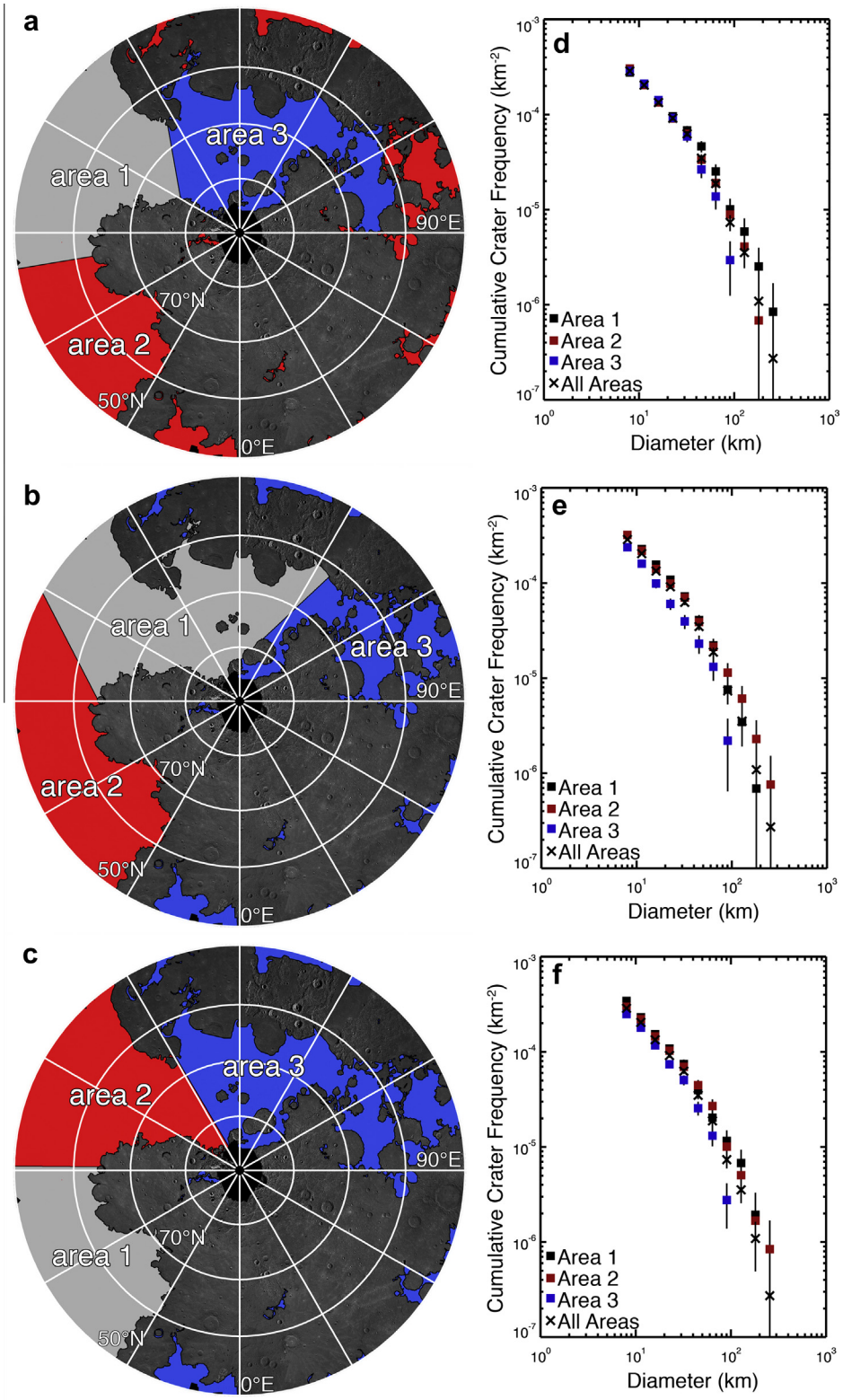

Fig. 3. Subdividing the NHCT (3.67×10^6 km^2 measurement area) into three approximately equal regions (areas provided in Appendix A, Table A1) does not reveal statistically distinguishable cumulative SFDs for impact craters. (a–c) Three alternative subdivisions of the NHCT and (d–f) their corresponding cumulative SFDs, plotted against the entire NHCT distribution for comparison.

Additionally, there are partially filled craters with and without rim breaches within the NSP (Fig. 7b and c) and in the NHCT near the NSP unit boundary (Fig. 7c).

All but a small region of the rim of the Goethe basin (81.50°N, 306.17°E, 317 km diameter) was buried by smooth plains material, and well-formed arcuate wrinkle ridges within these plains demarcate the buried rim (Fig. 8a and d). With the morphological relationships derived by Pike (1988), we estimate the Goethe basin rim height to have been >2.2 km and the original basin depth to have exceeded 4 km. Additional wrinkle ridges deform the smooth

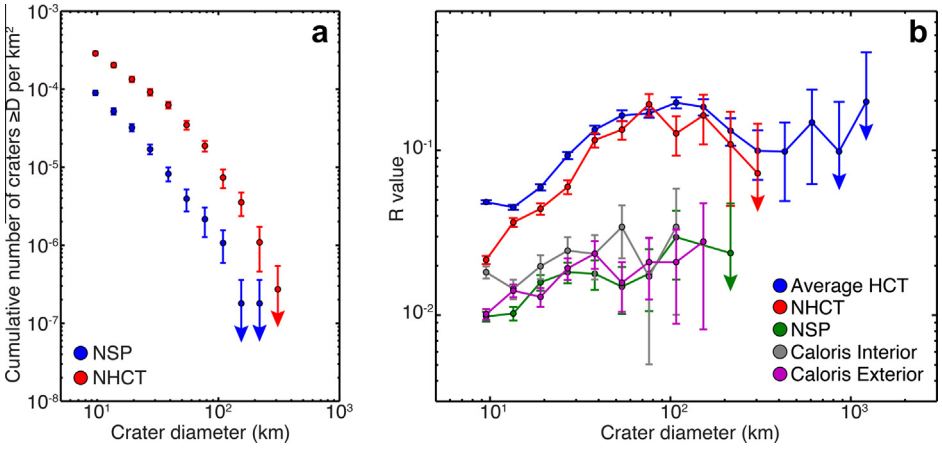

Fig. 4. (a) Cumulative SFD and (b) R plot for craters on the NHCT (3.67×10^6 km^2 measurement area) and post-plains craters on the NSP (5.59×10^6 km^2 measurement area). The NHCT has greater crater densities than the NSP. In (b), the distribution for the NHCT is compared with that for "average" heavily cratered terrain (9.04×10^6 km^2 measurement area; Strom et al., 2011), and the distribution for the NSP is compared with those for post-plains crater populations on the Caloris interior and exterior plains (1.94×10^6 km^2 and 4.75×10^6 km^2 measurement areas, respectively; Strom et al., 2011). Uncertainty estimates are equal to the square root of the number of craters for a given bin, and arrows indicate diameter bins that include only a single crater. Tabulated data for the NHCT and the NSP post-plains crater populations are provided in Appendix A, Tables A3 and A5, respectively.

plains within the basin interior, and arcuate wrinkle ridges and interior fractures trace the rim location of two buried craters located near the basin center (Klimczak et al., 2012; Watters et al., 2012). These two buried craters have diameters of ~45 km and ~60 km, which implies that they had initial rim heights of ~0.9 km and 1.1 km and original crater depths of ~2.3 km and 2.7 km, respectively.

Unambiguous superposition relations are observed for many buried craters in the NSP and are not limited to the largest impact basins (Fig. 8; Head et al., 2011). Tung Yuan crater (75.22°N, 296.51°E, 60 km diameter) superposes an unnamed basin (76.21°N, 284.16°E, ~250 km diameter), for which original rim height and interior depth are estimated to be greater than 2.2 km and 4 km, respectively (Fig. 8b and e). There are two large (~40 km and ~55 km in diameter) craters buried near the basin rim, with estimated rim heights of ~0.9 km and 1.1 km and original crater depths of ~2.2 km and 2.6 km, respectively. Within the basin, numerous smaller craters (~10–35 km in diameter) are partially or completely buried. We estimate that these craters originally had rim heights between ~0.4 km and ~0.8 km and depths between ~1.3 km and 2.1 km. Egonu crater (67.40°N, 60.80°E, 25 km diameter) superposes an unnamed basin (66.60°N, 60.86°E, ~155 km diameter; Fig. 8c and f) with an estimated original rim height of 1.8 km and a depth greater than 4 km. The basin interior contains one large buried crater (~80 km in diameter), with an estimated rim height of 1.3 km and an initial depth of 3.1 km. The buried crater is offset from the basin center, and there are graben collectively arrayed in a polygonal pattern within the crater's interior.

In addition, there is evidence for widespread burial of craters in the diameter range 4–25 km (Figs. 9 and 10; Head et al., 2011; Klimczak et al., 2012). We confidently identified 285 buried craters in this smaller size range, although additional buried craters may exist (Section 2.2). The steep decrease in the number of craters at less than 10 km diameter likely reflects a sampling bias at these smaller diameters, in addition to the preferential burial of smaller craters relative to larger craters during volcanic flooding (smaller craters contain smaller volumes to fill; Fig. 11). Estimates of rim height and interior crater depth for buried craters in the diameter range 4–25 km are ~0.2–0.7 km and ~0.8–2.0 km, respectively. The smaller buried craters are not limited to flooded crater interiors; such features are frequently observed in the NSP among and between the larger buried craters (Figs. 9 and 10).

3.3.2. Size–frequency distributions for buried craters

Buried craters are widespread and broadly distributed across the NSP. The total number of buried craters, particularly for smaller diameters (<30 km), is likely to be greater than reported here, because of limitations on identification imparted by illumination conditions (as discussed in Section 2.2). Furthermore, particularly because of the different crater degradation states existing on the surface before burial (Section 2.3), craters of a wide range of sizes likely were buried to sufficient depth to render them unrecognizable.

Craters as large as ~260 km in diameter were fully buried by the emplacement of the NSP. For the buried craters, $N(10) = 79 \pm 5$ and $N(20) = 42 \pm 3$. The cumulative SFDs of the NSP post-plains craters, buried craters, and NHCT are markedly different (Fig. 12). At diameters less than 30–60 km, the buried crater cumulative SFD slope shoals and begins to converge with the post-plains population at 8–10 km diameter (Fig. 12a). The slope of the cumulative SFD for buried craters is distinct from those for the post-plains and NHCT populations at ~30–100 km diameter and is statistically indistinguishable from that for the NHCT at ~100–130 km diameter. Similar to the post-plains crater population, the cumulative SFD for buried craters exhibits no distinct kinks (Fig. 12a). The R plot shows that the SFD for the buried crater population has a similar shape and slope as that for the NHCT crater population, particularly for diameters ⩽60 km, but a lower overall crater density for diameters ⩽150 km (Fig. 12b).

3.4. Thickness and volume estimates for the NSP

From the diameters of buried craters we have estimated the regional depth of flooding as a means to estimate the thickness of the NSP. Rim height estimates for embayed craters with <25% rim remaining (8–157 km in diameter) range from ~0.4 to 1.8 km. For this diameter range, original crater depths are estimated to have been between 1.6 km and >4 km. This range indicates the thickness of volcanic deposits required at the local scale to bury completely craters 8–157 km in diameter. However, although we identified ~300 buried craters in the 4–25 km diameter range, difficulties in confidently measuring the true population of these smaller craters (Section 2.2) prompted us to adopt 25 km as a minimum diameter for estimating thickness and volume for the NSP. The smallest and largest completely buried

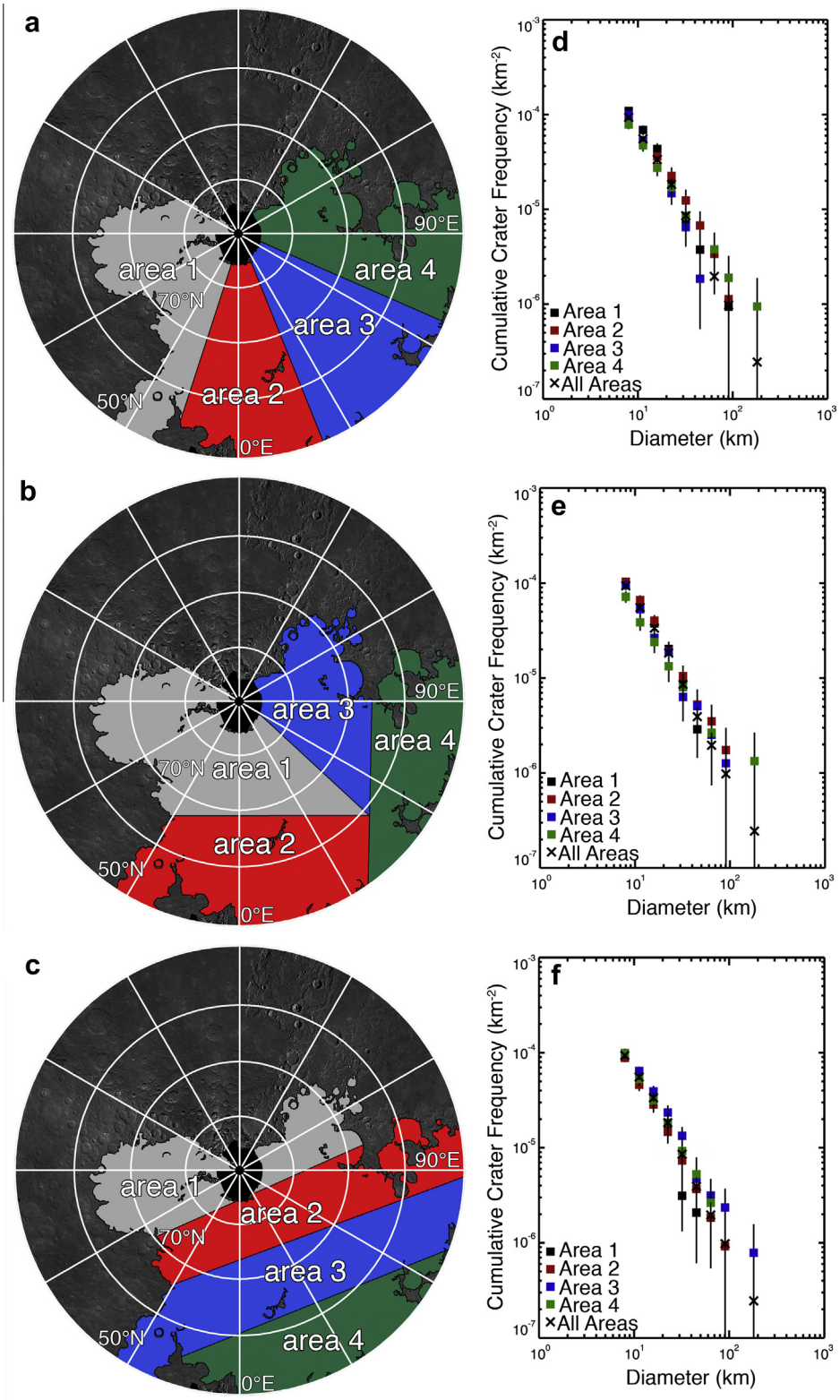

Fig. 5. Subdividing NSP1 (4.08×10^6 km^2 measurement area) into four approximately equal regions (areas provided in Appendix A, Table A2) does not reveal statistically distinguishable subunits in cumulative SFDs for post-plains impact craters. (a–c) Three subdivisions of the NSP and (d–f) their corresponding cumulative SFDs plotted against the entire NSP distribution for comparison.

craters, then, at diameters of 25 km and 157 km, respectively, have estimated rim heights of ~0.7 km and ~1.8 km, respectively. This thickness range agrees with that given by Head et al. (2011). Locally, NSP thickness may be greater (or less), depending on the sizes of craters, their pre-burial degradation state, and the depth of their interior flooding.

Ranges in the volume of the NSP may be derived from this range in burial depths. For an area inclusive of all NSP units (NSP1 and

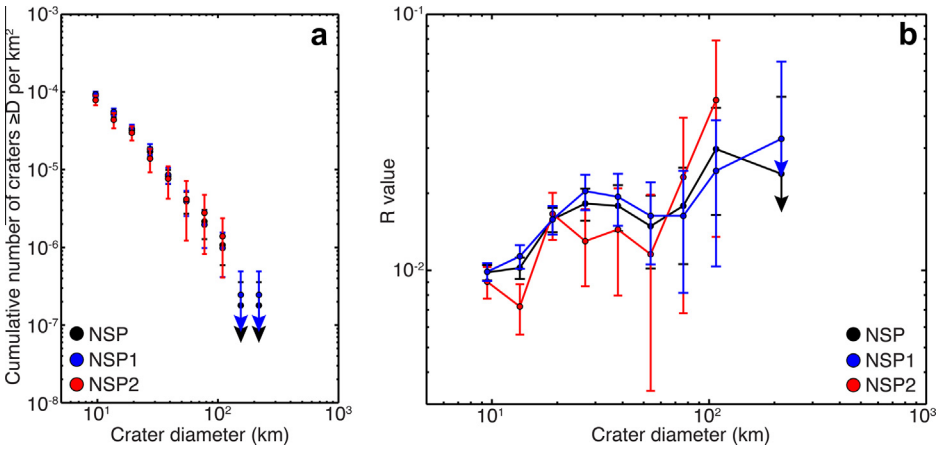

Fig. 6. (a) Cumulative SFD and (b) R plot for the NSP post-plains crater population (5.59×10^6 km^2 measurement area) plotted for the two subareas, NSP1 (4.08×10^6 km^2 measurement area) and NSP2 (1.51×10^6 km^2 measurement area) and for the NSP overall. NSP1 and NSP2 are statistically indistinguishable on the two plots. Uncertainties are equal to the square root of the number of craters for a given bin, and arrows indicate diameter bins that include only a single crater. The NSP2 SFD exhibits larger uncertainties because of the smaller measurement area.

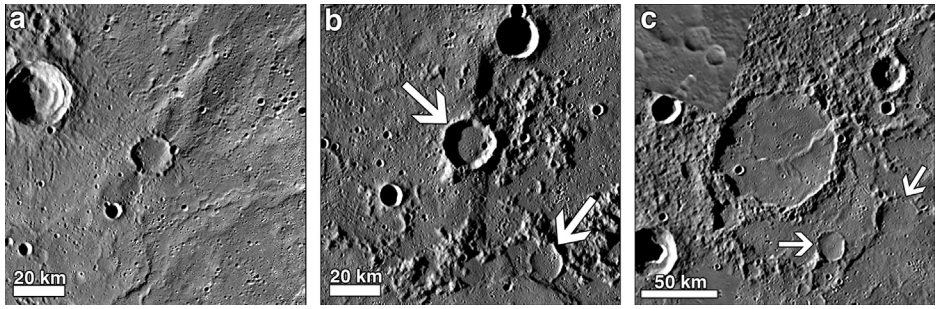

Fig. 7. (a) Embayed crater in the NSP (77.79°N, 246.59°E, ~18 km diameter), with only the crater rim exposed at the surface. (b) Crater (82.59°N, 274.18°E, ~20 km diameter, arrow near center) in NHCT embayed by NSP. A second embayed crater (~15 km diameter) is noted with an arrow at the lower right. (c) Crater located at a boundary between NHCT and NSP (image center is at 61.09°N, 328.58°E, and the crater is ~80 km in diameter) and partially embayed by smooth plains material within the crater interior. Two unnamed smaller craters (arrows, lower right) were also embayed and nearly buried by smooth plains material. From MDIS WAC monochrome mosaic, 400 m per pixel.

NSP2; 5.59×10^6 km^2) and under the assumption that NSP2 hosts a population of buried craters similar to that in NSP1, we estimate that a conservative volume for the NSP material is between 4×10^6 km^3 and 10^7 km^3.

3.5. Areal density of craters on the NSP

A map of areal density for post-plains impact craters on the NSP is shown in Fig. 13. Areas have been divided into regions of high, moderate, and low crater density (Section 2.4; Fig. 14). The "moderate" density class includes ~81% of the sample population, whereas the "high" and "low" density classes are defined by the upper and lower 10th percentiles, respectively. Representative regions corresponding to the area of a single neighborhood were selected from within the three density types in the NSP to determine the average $N(4)$ value, $N(4)_{avg}$, for high-, moderate-, and low-density regions (Table 2). Most of the NSP, not surprisingly given the definition, is characterized by a moderate areal density: $N(4) = 224–316$, or 44–62 craters per neighborhood; see Fig. 14c and d. There are three broadly circular regions of lower density and large, relatively isolated regions of higher density (Fig. 13). The measured areal density distribution for the NSP is similar to synthetic areal density maps derived from random point distributions created with the measured crater density of the NSP (Figs. 13 and 15; Section 2.4).

Table 2
Average crater density $N(4)$ in the northern smooth plains.

Density class[a]	Minimum $N(4)$	Maximum $N(4)$	Average $N(4)$
High	267	454	359
Moderate	214	328	273
Low	116	240	170

[a] Three circular regions with a radius of 250 km were selected within a given density-class region for averaging; each neighborhood may contain some output cells from other density classes.

In regions of high density, $N(4)_{avg}$ is 359 (70 craters per average neighborhood), and in regions of low density, $N(4)_{avg}$ is 170 (33 craters per average neighborhood). The large, relatively isolated high-density regions are located throughout the NSP (Figs. 13 and 14a, b). One high-density region (centered at 56.20°N, 211.21°E) is geographically proximal to Strindberg crater (189 km in diameter; 53.21°N, 223.44°E) and contains secondary craters that meet the mapping criteria (circular, non-overlapping, $D \geqslant 4$ km). However, the remaining high-density regions do not exhibit similar relationships with the surroundings. Regions of low-density might be expected to be found in the presence of comparatively recent volcanic features, but no volcanic vents, flow fronts, or embayment relations are observed on the surface in the vicinity of these regions. Instead, the well-defined circular regions of lower crater density are geographically associated with

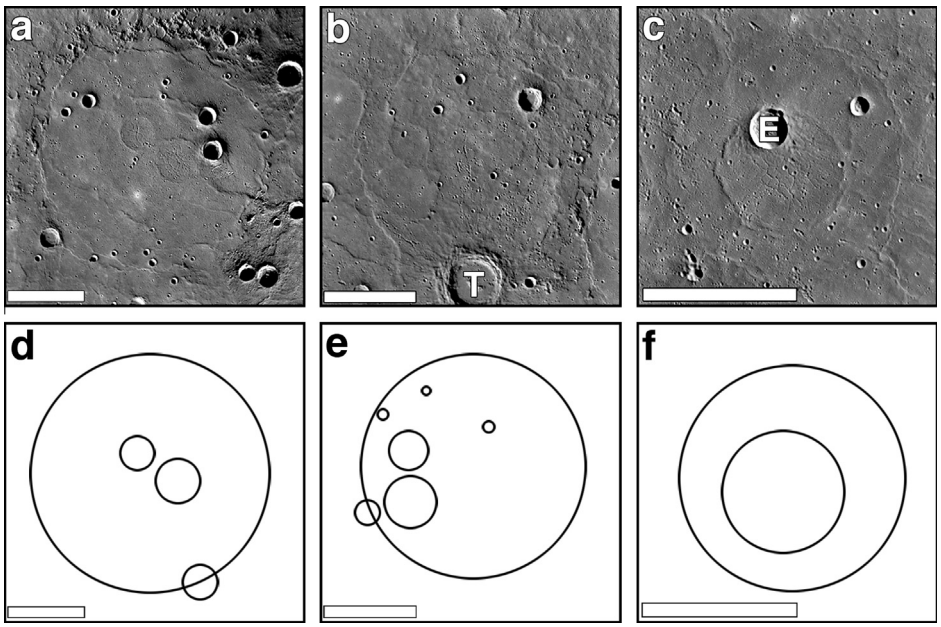

Fig. 8. (a–c) Examples of buried craters within the interiors of larger buried craters and basins, and (d–f) corresponding sketch maps of buried crater rims and those of their host basins. Scale bars are 100 km. (a and d) Goethe basin (81.50°N, 306.17°E, D = 317 km) displays a partially buried rim and encloses two buried craters near the basin center (D = ~45 km and 60 km). (b and e) Unnamed basin (76.21°N, 284.16°E, D = ~250 km) located to the east of Goethe and superposed by Tung Yuan (T) crater (75.22°N, 296.51°E, D = 60 km). Two large craters (D = ~45 km and 60 km) and numerous smaller craters (D = ~10–35 km) are buried within the basin interior. (c and f) Unnamed basin (66.60°N, 60.86°E, D = ~150 km) superposed by Egonu (E) crater (67.40°N, 60.80°E, D = 25 km). The basin interior contains one large buried crater (D = ~80 km) that is offset from the basin center and hosts interior tectonic features.

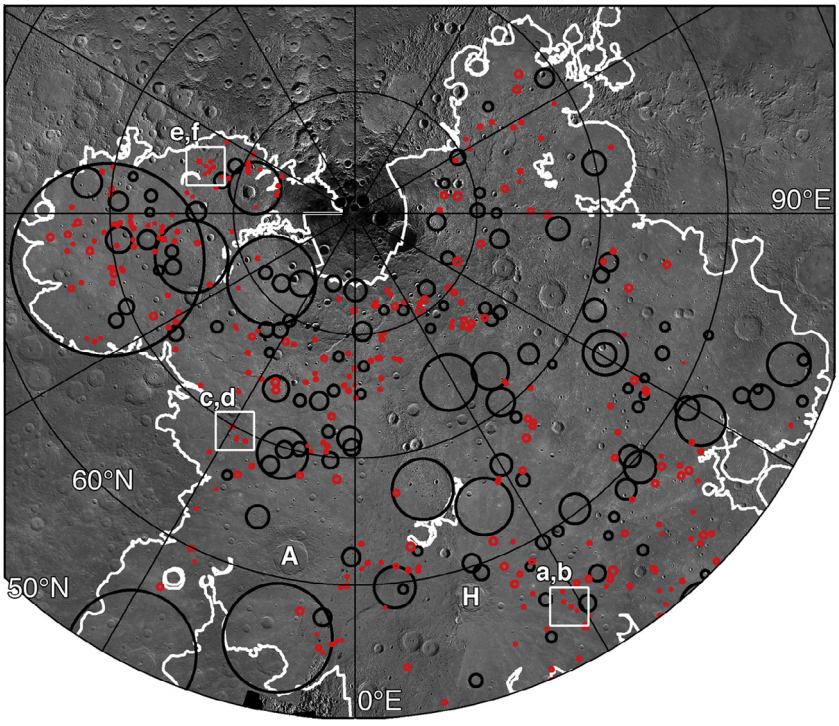

Fig. 9. Partially to fully buried craters in the NSP; red circles denote buried craters 4–25 km in diameter, and black circles denote larger ($\geqslant$25 km in diameter) buried craters and basins. The small buried craters are distributed widely across the NSP and provide evidence for multiple stages of volcanic activity. The three white boxes indicate the locations of the detailed views in Fig. 10. Abedin (A, 61.76°N, 349.35°E, D = 116 km) and Hokusai (H, 57.75°N, 16.90°E, D = 114 km) craters are marked for orientation.

the surface modification resulting from three large, relatively recent impact craters: Rustaveli [$N(4)_{avg}$ = 130], Abedin [$N(4)_{avg}$ = 187], and Hokusai [$N(4)_{avg}$ = 194]. In these areas, crater formation and emplacement of ejecta resurfaced a portion of the NSP and obscured the post-plains cratering record (Fig. 14e and f).

4. Discussion

4.1. NHCT: part of the global intercrater plains

When divided into arbitrary regions, some portions of NHCT (Fig. 3a and d; areas 1 and 2 in Fig. 3b, c, e, and f; Appendix A,

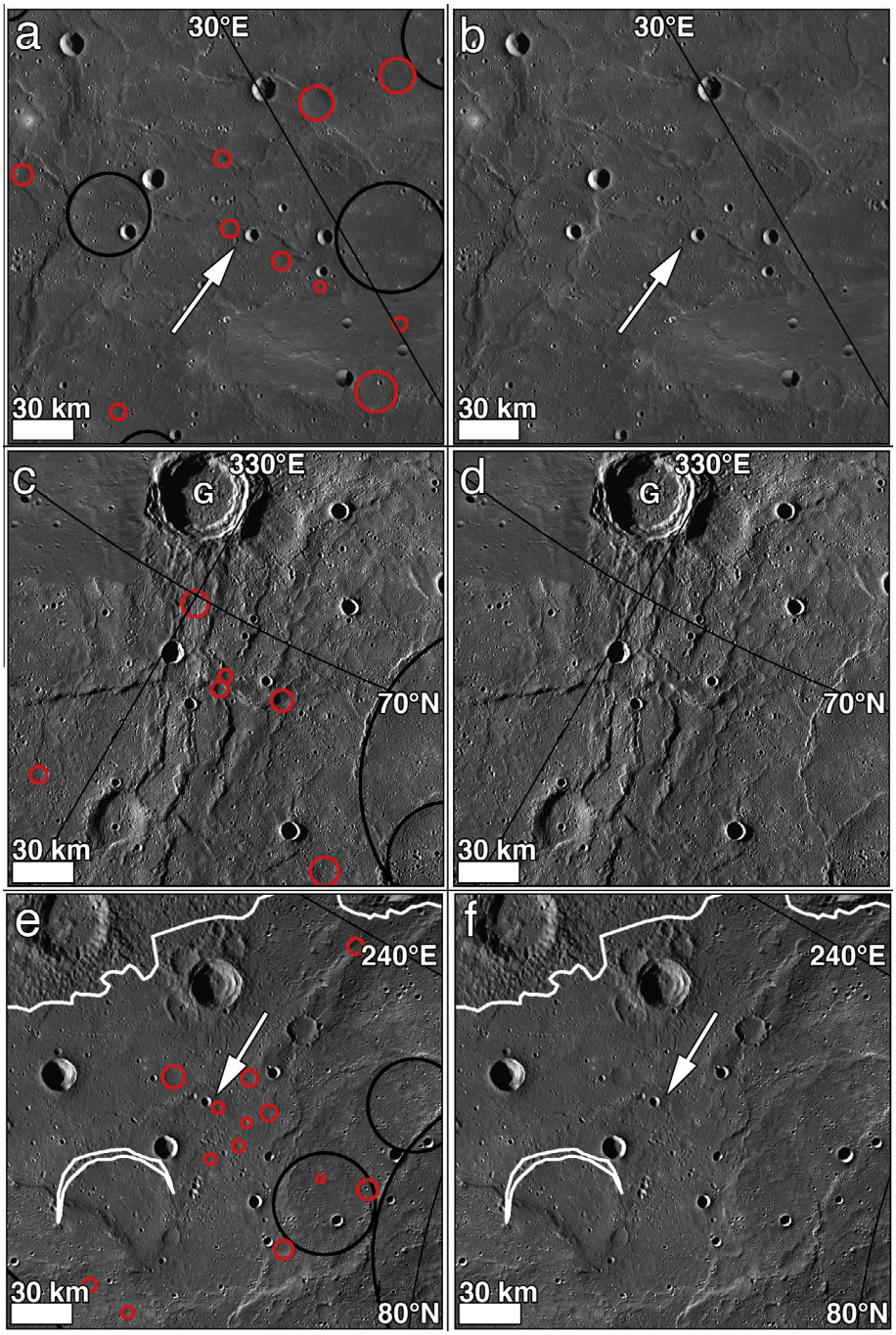

Fig. 10. Detailed views of three representative NSP locations with small (4–25 km diameter; red circles) and larger (⩾25 km diameter, black circles) buried craters noted. (a and b) Small buried craters to the east of Hokusai. The image is centered at 54.80°N, 28.19°E; a post-plains crater ~7 km in diameter is located adjacent to a buried crater ~9 km in diameter (white arrow). (c and d) Substantial tectonic deformation marks this area south of Grotell crater (G, 71.11°N, 328.24°E, D = 48 km), and several small buried craters are sharply defined by wrinkle ridges (image centered at 69.16°N, 332.23°E, on the buried crater doublet, ~7 km and ~8 km in diameter). (e and f) Small buried craters near the NSP–NHCT boundary, centered on a buried crater ~6 km in diameter adjacent to a post-plains crater ~5 km in diameter at 77.13°N, 252.35°E (white arrow).

Table A1) are statistically indistinguishable on the basis of the crater SFD, particularly at the smaller diameters. However, two arbitrary divisions of NHCT create a region with a lower crater density than the others (area 3 in Fig. 3b, c, e, and f). The lower crater density for area 3 compared with areas 1 and 2 for those two divisions (Fig. 3b, c, e, and f) could be interpreted as indicating that area 3 in each case is a statistically resolvable sub-unit within the NHCT. Although such an interpretation may have a statistical basis, it is unlikely, on morphological grounds, that either area 3 represents a younger NHCT region than the corresponding areas 1 and 2. Area 3 in each case is more strongly affected by NSP embayment than areas 1 or 2; smooth plains emplacement created several discontinuous regions of NHCT. The modification of NHCT by NSP emplacement removed part of the NHCT crater population, as evidenced by incompletely filled NHCT craters at the NHCT–NSP boundary and flooded craters connected by broad valley-like pathways (Fig. 3b and c). The dissection of the NHCT by NSP in each area 3 results in a decreased crater density for this subarea.

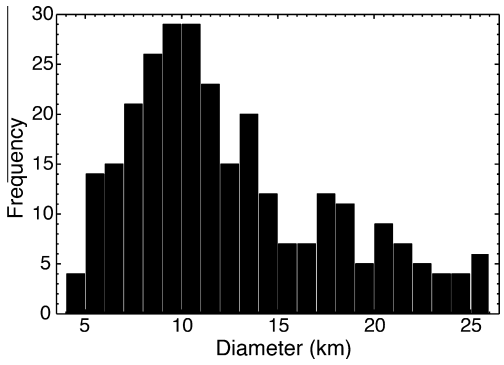

Fig. 11. Histogram of the number of buried craters versus diameter in the 4–25 km diameter range; a total of 285 buried craters have been identified. The sharp drop-off at diameters less than 10 km reflects the increasing difficulty of confidently identifying buried craters. For this mapped population, the median diameter is 11.1 km, the average diameter is 12.5 km, and the standard deviation is 5.2 km.

However, when portions of the discontinuous and modified regions of NHCT are included with the larger contiguous units (Fig. 3a), the cumulative SFDs for the three subareas are statistically indistinguishable, indicating that the cumulative SFD for each area 3 in Fig. 3b and c has been substantially affected by NSP embayment and NHCT crater burial.

Both the cumulative SFD and R plots show that the NHCT is older than the NSP (Fig. 4). Additionally, the R plot shows that the NHCT crater density for $D > 40$ km is statistically indistinguishable from that of the global average of heavily cratered terrain (Fig. 4b). However, for $D < 40$ km, although the NHCT exhibits a similar downward-sloping crater density in the R plot, it is statistically distinct from the global average of heavily cratered terrain (Fig. 4b) (Strom et al., 2008, 2011; Fassett et al., 2011). The overall trend of the NHCT in the R plot, with crater density increasing with diameter from $D = 8$ km to ~80 km and then leveling off until it decreases with increasing diameter for $D \geqslant$ ~110 km (Fig. 4b), is broadly consistent with the presence of a global distribution of terrain with a similar cratering history, equivalent to the average heavily cratered terrain of Strom et al. (2011). Moreover, the overall shape of the NHCT in the R plot is consistent with that observed for other heavily cratered surfaces in the inner Solar System (Strom et al., 2005). This similarity suggests that the same impactor population (so-called Population 1) is responsible for the regions of heavily cratered terrain observed on inner Solar System bodies.

The differences in crater density between the NHCT and average heavily cratered terrain elsewhere on Mercury (Fig. 4b) are likely the result of the distinctive resurfacing history for the NHCT. The downturn in the NHCT SFD at crater diameters <40 km is a function of differences in the degree of resurfacing relative to average heavily cratered terrain. This difference is statistically robust and consistent with other observations of a similar downturn for other local regions of Mercury, suggesting that resurfacing varied regionally in its extent (Strom et al., 2008, 2011). Morphological observations of embayed and filled craters within the NHCT support the removal of smaller craters by volcanic resurfacing or impact-related basin ejecta emplacement (i.e., deposits comparable to the Cayley Plains on the Moon; Wilhelms, 1976; Oberbeck et al., 1977). These local variations in crater density within NHCT indicate that at least one interval of widespread resurfacing occurred prior to emplacement of the NSP. Such an interval may have been marked by continuous or punctuated activity, either local volcanic resurfacing or basin ejecta emplacement (e.g., resulting from the Caloris impact), and distinguishing between these sources with the available data is not possible. Strom et al. (2011) interpreted crater density differences among different heavily cratered regions to reflect different contributions of intercrater plains emplacement, under the assumption that most intercrater plains are volcanic in origin. This interpretation is supported by recent analyses of MESSENGER orbital data with new criteria for the identification of intercrater plains developed on the basis of morphology, spectral properties, impact crater densities, and topography (Whitten et al., 2014).

Furthermore, previous work with Mariner 10 data (notably Strom, 1977), MESSENGER flyby data (e.g., Strom et al., 2011; Fassett et al., 2011), and MESSENGER orbital data (Marchi et al., 2013) involving comparisons of the crater SFDs of heavily cratered surfaces on Mercury to that for the lunar highlands showed that both geologic units have higher crater densities than other surfaces on their respective bodies, although the most heavily cratered regions on Mercury have lower crater densities than the lunar highlands (Fassett et al., 2011; Marchi et al., 2013). The high crater densities of these heavily cratered surfaces, which are dominated by the Population 1 craters of Strom et al. (2005, 2008, 2011), indicate that these surfaces likely date from the Late Heavy

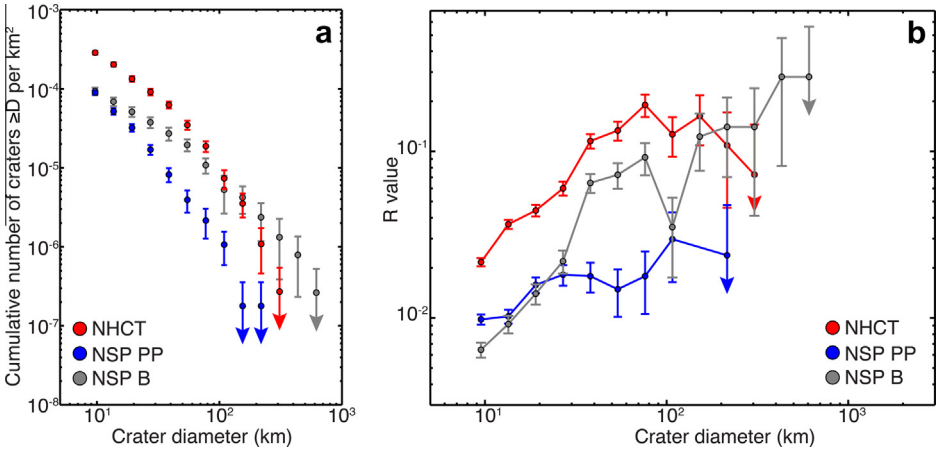

Fig. 12. (a) Cumulative SFD and (b) R plot for the NHCT (3.67×10^6 km^2 measurement area), NSP post-plains (NSP PP, 5.59×10^6 km^2 measurement area), and NSP buried (NSP B, 3.79×10^6 km^2 measurement area, selected from within NSP1 to exclude Rustaveli impact materials) crater populations. On the cumulative SFD plot, the buried crater population has a lower density than the NHCT and a higher density than the NSP for diameters ⩽130 km. On the R plot, the buried crater population has a lower SFD than the NHCT but a similar slope for diameters ⩽60 km. Uncertainties equal the square root of the number of craters for a given bin, and arrows indicate crater diameter bins with only a single crater. Tabulated data for the NHCT, NSP post-plains, and NSP buried crater populations are provided in Appendix A, Tables A3–A5, respectively.

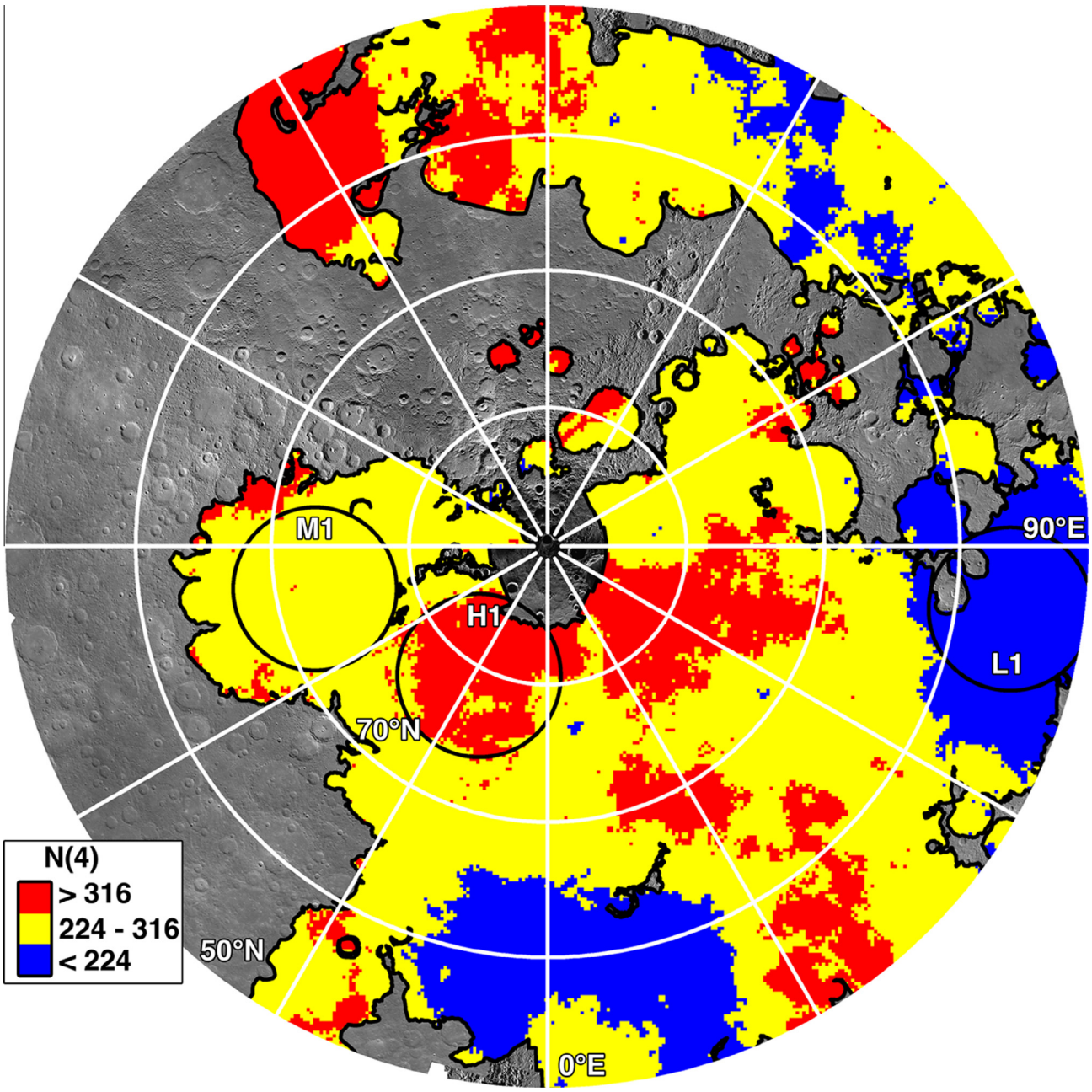

Fig. 13. Map of areal density of post-plains impact craters for the NSP in Lambert equal-area projection (neighborhood radius = 250 km, output cell = 10 km, $D \geqslant 4$ km). Black circles with 250 km radius represent example neighborhood areas for low (L1), moderate (M1), and high (H1) densities (Fig. 14). The color-coded classification was determined from a calculation of Poisson probabilities for the measured crater population and agrees with a statistical assessment of neighborhood size selection (Section 2.4). No boundaries between areas of distinct areal density are interpreted to be volcanic in origin; low-density regions correspond to areas resurfaced by crater formation and ejecta emplacement.

Bombardment (LHB) of the inner Solar System. Additionally, the large-scale resurfacing of the NHCT, by volcanic or basin ejecta emplacement (or both), must have occurred during the LHB because the resurfaced area, represented by a slightly lower crater density at diameters ⩽50 km, still retains the shape of the Population 1 crater distribution, despite the addition of the more recent post-LHB Population 2 craters (Strom et al., 2005, 2008, 2011).

4.2. NSP: young and regionally distributed

The cumulative SFD and R plot for post-plains craters on the NSP reveal a lower crater density than for the NHCT, so the NSP constitutes a younger geologic unit (Fig. 4). The SFDs of NSP1 and NSP2 are indistinguishable (Fig. 6), enabling us to combine these two NSP regions for statistical treatment (Fig. 6). No statistically separable subunits are revealed when arbitrary subareas are selected (Fig. 5; Appendix A, Table A2), indicating that the NSP may be interpreted as having been emplaced over a geologically brief interval of time.

The relatively low density and flat distribution for the NSP post-plains crater population on an R plot (Fig. 4b) indicate that these craters are predominately Population 2 (Strom et al., 2005; Fassett et al., 2011; Head et al., 2011). When compared with the Caloris interior and exterior post-plains crater populations (Fig. 4b), the NSP post-plains population has a similar crater density and slope (and thus age) to the Caloris plains. Previous work showed that the Caloris plains postdate basin formation (e.g., Spudis and Guest, 1988; Murchie et al., 2008; Fassett et al., 2009;

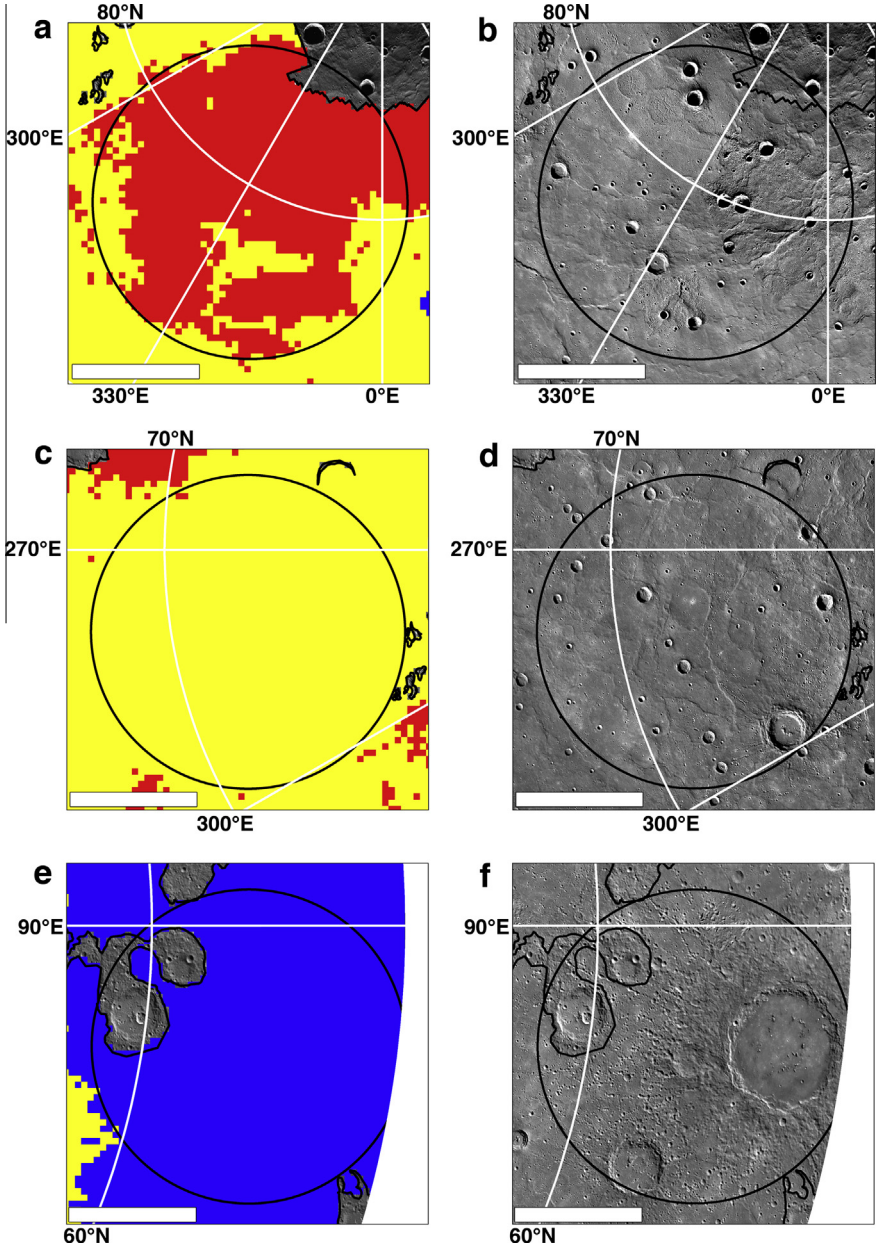

Fig. 14. (a–f) Example areas of high, moderate, and low areal density of post-plains impact craters for the NSP, identified in Fig. 13 as H1, M1, and L1, respectively. (a, c, and e) Maps of areal density; the color-coding classification is the same as in Fig. 13, and black circles denote one neighborhood area (250 km radius). (b, d, and f) MDIS monochrome WAC mosaics of the same areas; white scale bars are 200 km in length. (a and b) An isolated high-density region, in which there are no evident geologic boundaries indicative of resurfacing. (c and d) An area of moderate density, as is typical of the NSP. (e and f) Low-density regions are attributed to modification by ejecta from large post-plains impact craters; Rustaveli (52.54°N, 82.59°E, D = 200 km) is the largest example in the NSP.

Denevi et al., 2013a) and were likely emplaced near the end of the LHB (e.g., Strom et al., 2008, 2011). More recent mapping of additional major smooth plains units interpreted to be volcanic (i.e., Rudaki plains, south of Rachmaninoff, and those within Beethoven and Rembrandt) revealed a limited range of crater retention ages (Fassett et al., 2012; Denevi et al., 2013a) that also overlap those of the Caloris plains (Spudis and Guest, 1988; Strom et al., 2008; Fassett et al., 2009, 2012; Denevi et al., 2013a). The overlap in uncertainty estimates for all major smooth plains units indicates that their relative ages are statistically indistinguishable from that for the NSP. Thus, any further statistical variation in emplacement time among the geologic units cannot be assessed beyond concluding that the NSP, the Rudaki plains, the smooth plains south of Rachmaninoff, and those associated with Beethoven, Rembrandt, and Caloris basins formed more or less contemporaneously.

As noted above, when a portion of a planetary surface is resurfaced (by ejecta emplacement or volcanism), the erasure of craters may be manifested as kinks in the cumulative SFD for the superposed crater population (e.g., Neukum and Horn, 1976; Hiesinger et al., 2002), particularly if the time interval between initial emplacement of material and resurfacing was long. Recent investigations suggest that resurfacing events with time differences from 0.5 Gy to nearly 3 Gy are observable in the SFDs for regions on Mars (e.g., Williams et al., 2008; Michael and Neukum, 2010; Neukum et al., 2010), but estimates for the difference in age between the original surface and the resurfacing event from the cumulative SFD are poorly constrained. The NSP cumulative SFD for the post-plains crater population does not exhibit kinks (Fig. 4a) even though buried craters are visible. It may be that the interval(s) between episodes of resurfacing in the NSP were

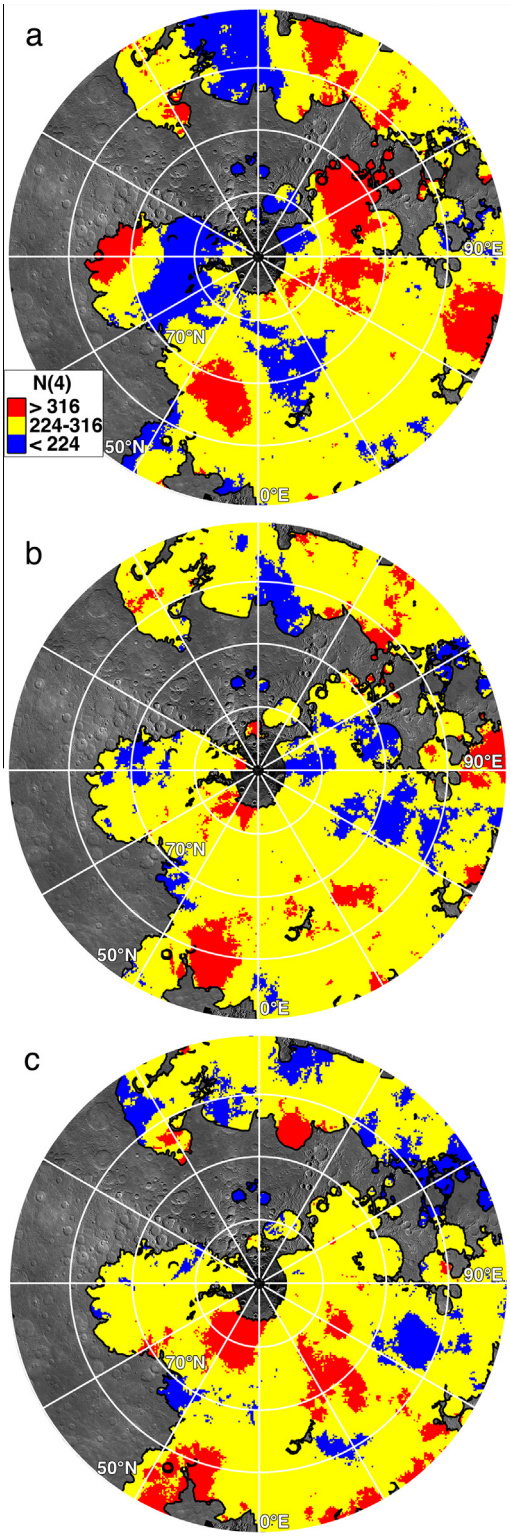

Fig. 15. (a–c) Three synthetic areal density maps for post-plains impact craters on the NSP determined from different random distributions, each containing 1500 points. Output cell is 10 km; neighborhood radius is 250 km. Colors are assigned according to the upper and lower 10th percentiles, as well as the remaining ~81% of the distribution, calculated from the Poisson probabilities (Section 2.4).

not of sufficient length to allow a statistically appreciable number of craters with $D \geqslant 8$ km to form and contribute kinks in the cumulative SFD. For instance, an investigation in Mare Imbrium on the Moon did not show distinct kinks in the cumulative SFD

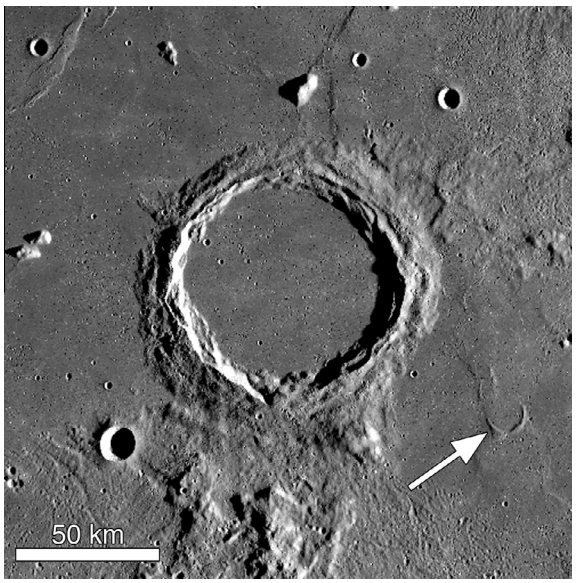

Fig. 16. Archimedes crater (29.72°N, 356.01°E, D = ~80 km), located in eastern Mare Imbrium on the Moon, is filled with volcanic smooth plains materials (mare basalt). Mare basalt flows embayed Spurr crater (arrow; 27.92°N, 358.74°E, D = ~13 km) so that only half of the crater rim is presently visible. LROC WAC monochrome mosaic, 400 m per pixel, illumination from the right.

for units with model age differences of less than ~300–500 My (Ostrach and Robinson, 2014) despite identification of several geologic units with statistically separable model ages (Hiesinger et al., 2000; Bugiolacchi and Guest, 2008). Or, equally plausible, a late-stage volcanic emplacement episode may have nearly completely resurfaced the NSP up to the largest diameters, in which case the cumulative SFD records only the post-plains craters formed since the most recent resurfacing of the region, and no kinks would be expected.

4.3. Absolute age of the NSP

At present, there are three principal chronologies for Mercury. Neukum et al. (2001a, 2001b) updated the absolute chronology for Mercury originally derived by Strom and Neukum (1988) by incorporating newer data related to asteroid populations, a cratering rate scaled from that of the Moon, and improvements in crater scaling models. With the Neukum et al. (2001b) chronology and the crater SFDs of this study, the NSP have an absolute model age of 3.7 ± 0.01 Ga, where the quoted uncertainty includes only counting statistics and neglects systematic uncertainty in the chronology function, which is several hundred million years. This age for the NSP is consistent with previous results (Head et al., 2011) and for other major regions of smooth plains having estimated ages of ~3.7–3.9 Ga (Denevi et al., 2013a), which were derived with the Strom and Neukum (1988) chronology.

More recently, two alternative model production functions (MPFs) have been developed that incorporate additional parameters (e.g., modeled relative global impact fluxes, revised crater scaling, two impactor populations, target-specific properties) and newer data (Marchi et al., 2005, 2009, 2011; Le Feuvre and Wieczorek, 2011). The MPF calculated by Marchi et al. (2009, 2011) results in a model age for the NSP of 2.5 ± 0.3 Ga, and the χ^2 test used to assess the MPF fit favors an anchor to intermediate crater sizes (S. Marchi, personal communication, 2012). The MPF of Le Feuvre and Wieczorek (2011) yields a model age of 3.30 ± 0.3 Ga for the Caloris interior plains, and on the basis of the close similarity of the NSP post-plains crater population to the Caloris interior

Table 3
Absolute model ages for the northern smooth plains.

Model production function	Model age (Ga)
Neukum et al. (2001b)	3.7 ± 0.01[a]
Le Feuvre and Wieczorek (2011)	3.30 ± 0.3
Marchi et al. (2009)	2.5 ± 0.3

[a] Formal statistical uncertainty estimates.

plains crater population (Fig. 4b), the best model age estimate with this MPF is also 3.30 ± 0.3 Ga. This age is for a combination of porous ("megaregolith", or highly fractured material) and non-porous ("hard rock", or competent material) targets to estimate scaling of craters from impactor dimensions; an older age (~3.7 Ga) would be derived with only porous scaling, and a younger age (~2 Ga) would be derived with only non-porous scaling. Table 3 summarizes the absolute model ages for the three MPFs.

For comparison, from Mariner 10 observations of the Caloris interior plains, a crater density of $N(20) = 39 \pm 12$ was determined by Spudis and Guest (1988) and a model age of 3.85 Ga was inferred for a lunar-like impact flux for Mercury (Strom and Neukum, 1988). Given that the crater SFDs for the NSP and Caloris plains are statistically indistinguishable, an absolute model age of ~3.85 Ga would be assigned to the NSP under the Strom and Neukum (1988) MPF.

The wide range in estimates for the absolute age of the NSP among the three model age chronologies as well as the older calculation from Mariner 10 observations indicates that more work is required for estimates of crater production and their uncertainties for the inner Solar System, particularly since there are no known samples of Mercury in our meteorite collections. However, on the basis of most current estimates for the cratering rate of Mercury, these plains units formed approximately contemporaneously with the main epoch of mare emplacement on the Moon: after the period of heavy bombardment and at least several billion years before the present.

4.4. Buried craters: evidence for volcanic resurfacing

4.4.1. Morphological relations

Embayment relations provide abundant evidence for volcanic emplacement of plains material (e.g., Head et al., 2009a). In the NSP and near NHCT-NSP boundaries there are partially flooded craters (Fig. 7c) that are morphologically similar to Archimedes crater on the Moon (Fig. 16). These crater embayment and infilling relations are defined by the stratigraphic relationships between an impact crater and nearby volcanic smooth plains units. Archimedes is the type example (Fig. 16) of an impact crater at which mare material from the Imbrium basin embayed the Archimedes ejecta deposits and the crater interior was filled with mare material from a different source vent or vents, as indicated by the absence of an obvious breach in the crater rim and wall (Wilhelms and McCauley, 1971; Head, 1982).

Similar stratigraphic relationships between buried craters are observed within the NSP on Mercury (Fig. 8), and a comparison of estimated volcanic fill thickness provides compelling evidence for at least two periods of volcanic resurfacing (Head et al., 2011). The presence of buried craters ($\geqslant$25 km in diameter) within partially to completely buried larger craters and basins lends support to the hypothesis that multiple phases of smooth plains emplacement occurred. Estimates of crater depths and rim heights (Pike, 1988) for three buried basins and their buried interior craters (Fig. 8) yield the following constraints. The original basin depths likely exceeded 4 km, indicating at least 4 km of volcanic fill in the basin interiors. The buried craters within the basins had original rim heights between 0.5 and 1.3 km. If those fully buried craters were flooded so that the rim was just barely covered by volcanic material, a minimum thickness of 1.3 km of volcanic material is required to bury the craters within the basins.

Since buried craters are observed, the thickness estimates suggest that these smaller craters must have formed on a thick fill that modified the original floor of their host basins. Although the greatest depth to which a crater can be buried by volcanic material and still concentrate tectonic deformation above its buried rim is not known, we infer that the rim heights of the buried interior craters, which are less than half the estimated basin depths, are insufficiently large to produce surface tectonic deformation from impacts onto the original floor of the host basin. Moreover, the presence of graben with multiple orientations in some flooded craters (e.g., those within Goethe basin, Fig. 8a) and their absence in neighboring craters of similar diameter (e.g., Fig. 8b) has been interpreted on the basis of finite element models as indicating different depths of volcanic flooding across the NSP during the most recent major episode of infilling (Freed et al., 2012; Klimczak et al., 2012; Watters et al., 2012). This inference supports the conclusion that the interior craters hosted by buried basins were not all buried to the same depth, e.g., the depth of the unfilled basin.

Therefore, if the finite element models for buried craters are representative of the subsurface geologic conditions within the NSP (Freed et al., 2012), then a first resurfacing episode was responsible for initial flooding of the larger basins, to an unknown depth, preferentially erasing small craters. It is plausible that basin ejecta contributed to resurfacing as well, in a manner similar to the Imbrium basin ejecta on the Moon (i.e., the Fra Mauro Formation; e.g., Wilhelms, 1987). The most likely candidate to provide a thick, regional fill of basin material is Caloris. The Odin Formation, mapped in the circum-Caloris region and composed of knobby plains, was interpreted as basin ejecta on the basis of Mariner 10 images (Murray et al., 1974a; Strom et al., 1975b; Trask and Guest, 1975). Although stratigraphic relations support the idea that the Odin Formation is composed of basin ejecta with portions embayed by younger volcanic deposits, crater size–frequency analyses are not consistent with the observed stratigraphic relations (Fassett et al., 2009; Denevi et al., 2013a). Moreover, the Odin Formation does not extend into the larger NSP region NSP1 (e.g., Fassett et al., 2009), where the buried crater population is observed, indicating that the basin ejecta deposits emplaced in this region were not substantial in volume. Aside from Borealis and Goethe, which both pre-date the plains, there are no basins in the north polar region unambiguously identified from MLA or MDIS data (Zuber et al., 2012; Fassett et al., 2012). Thus, we suggest that the observed resurfacing was largely by volcanic emplacement.

After initial resurfacing, there was an interval of time sufficient for major craters to have formed on the volcanic surface, which was subsequently covered by at least one later episode of plains emplacement. We suggest that the burial of craters identified in flooded basin interiors (Fig. 8) reflects at least a second volcanic resurfacing of the NSP, during which the basins and their interiors, including craters superposed on earlier plains material, were infilled and further buried. Additional evidence for this second volcanic resurfacing episode is the population of buried craters $\leqslant$25 km in diameter that is widely distributed across the NSP (Fig. 9). If the smallest buried craters were spatially limited in extent, then topographic variation on the pre-plains surface that underlies the NSP might account for their presence. For instance, if the smallest buried craters formed on a local topographic high they would be expected to cluster in a single location, but because the craters are dispersed throughout the NSP, it is improbable that all craters 4–25 km in diameter (285 were measured) are perched on former topographic highs. Further, the close proximity of these smaller buried craters to larger buried craters, particularly within

Borealis basin, suggests stratigraphic relations inconsistent with the smallest buried craters having formed on the pre-NSP surface. Moreover, the morphology of arcuate tectonic features interpreted to overlie the rims of the smallest buried craters is sharp and distinct (Fig. 10) across the NSP, regardless of location (e.g., proximity to the NHCT-NSP boundary or near the center of the NSP), suggesting that these smallest craters are not buried to substantially different depths (e.g., Freed et al., 2012; Watters et al., 2012). Volcanic plains ~0.2–0.7 km thick (average thickness ~0.5 km) are required to bury the smallest crater rims. Partially buried craters and kipukas near the NSP-NHCT boundary (presumably with thinner NSP than elsewhere; Fig. 10c) are consistent with a burial thickness of at least ~0.2 km to ~0.5 km. However, the larger buried craters in the central NSP (~70°N, ~30°E) require ~1.5 km to ~2 km of material to bury the rims, yet buried craters ⩽25 km in diameter persist with sharp morphology. Therefore, the smallest buried craters likely were flooded during a late (or final) stage of volcanic eruptions.

4.4.2. Size–frequency distributions for buried craters

The post-plains and buried crater populations exhibit a large range in diameters (as large as ~190 km, ~260 km, and ~680 km for the post-plains, fully buried, and partially buried crater populations, respectively), and the cumulative SFD for buried craters has a shallower slope than those for either the NSP or the NHCT (Fig. 12a). The shallow slope of the cumulative SFD for buried craters suggests that volcanic resurfacing removed a portion of the original buried crater population, an interpretation supported by observations of morphology. The crossover of the cumulative SFDs for the NHCT and buried crater populations at ~130 km diameter and the similar SFD slopes for diameters ~130–680 km (Fig. 12a) indicate that the buried crater population likely reflects embayment of the original NHCT surface. At ~60 km diameter, there is a step-like decrease in the density of buried craters with decreasing diameter as seen in the R plot (and as a shallower slope in the cumulative SFD) that reflects volcanic resurfacing (Fig. 12b, Section 2.2).

The absence of distinct kinks in the cumulative SFD, paired with the morphology, also supports the hypothesis that only a geologically brief interval separated the resurfacing episodes that affected the buried crater population. With the Neukum et al. (2001b) chronology, the entire buried crater population has an absolute model age of 3.8 ± 0.01 Ga. Similarly, the model age for the buried craters (D = 4–103 km) within the largest partially buried basin in the NSP (D = 678 km; centered at 69.91°N, 280.68°E) is 3.8 ± 0.02 Ga. Furthermore, when craters with D < 30 km are excluded, the buried crater population is 3.9 ± 0.02 Ga. This age, ~3.8–3.9 Ga for the buried crater population, reflects the oldest period of NSP emplacement. Similar results, albeit with different ages, are obtained with the model production functions of Marchi et al. (2009, 2011) and Le Feuvre and Wieczorek (2011). When only the population of small buried craters (D = 4–30 km) is considered, $N(10) = 47 \pm 3$ and $N(20) = 10 \pm 2$, and the model age is 3.7 ± 0.01 Ga. However, this age is the same as that determined for the NSP post-plains crater population, which must be younger as indicated by superposition relations and statistically separable $N(10)$ and $N(20)$ values. Therefore, on the basis of the absolute model ages determined from the Neukum et al. (2001b) chronology (and the inherent assumptions and systematic uncertainties included), the interval separating resurfacing episodes in the NSP may have been as brief as 100 My or less.

4.5. Volume of NSP material

From the geometry of buried craters, we have estimated the volume of the NSP to be at least 4×10^6 km^3 to 10^7 km^3. Such a large volume is consistent with the high-volume, high-effusion-rate style of volcanism predicted for Mercury (Wilson and Head, 2008, 2012). For comparison, the estimated volume for all lunar mare deposits is $\sim 10^7$ km^3 (Head and Wilson, 1992), and such large igneous provinces as the Columbia River flood basalts and the Deccan Traps on Earth are estimated to have volumes of 1.3×10^6 km^3 and 8.2×10^6 km^3, respectively (e.g., Coffin and Eldholm, 1994, and references therein). When compared with the largest-known flood basalts on Earth and Mars, at least the minimum values for the volume of the NSP are modest: the Hesperian Ridged Plains on Mars, which cover ~30% of the planet, have an estimated volume of $\sim 4 \times 10^7$ km^3 (Head et al., 2002), and the volume of the terrestrial Ontong Java large igneous province is estimated to be $\sim(4–8) \times 10^7$ km^3 (Coffin and Eldholm, 1994).

4.6. Areal density of impact craters in the NSP

Ostrach and Robinson (2014) used areal density measurements of impact craters as a means of identifying resurfacing boundaries originally identified as color units within Mare Imbrium on the Moon. Volcanic units with model age differences >300–500 My were successfully distinguished without employing multispectral data (Ostrach and Robinson, 2014). Multispectral color differences are absent (or currently undetectable) within the NSP, so the application of the areal density mapping technique allows us to search for subunits within the NSP that are distinguishable by crater retention age.

The NSP exhibit widespread areas of moderate areal density of impact craters, consistent with a randomly distributed crater population similar to the synthetic density maps derived from measured crater frequencies (Figs. 13 and 15). Three iterations of synthetic areal density maps all exhibit patchy areas of high and low density interspersed within a spatially extensive region of moderate density, indicating that such density variations are expected for a random distribution. Thus, although regions of high and low density observed in the measured areal density map are similar to those observed in the synthetic density maps, visual assessment of such areas must be made to determine if those regions represent geological differences rather than statistical fluctuations.

Photogeological observations confirm that areas with locally low crater density primarily result from impact-related modification of the NSP. The regions of low crater density reflect modification of the surrounding area to a distance of approximately two diameters from the crater rim by ejecta emplacement and secondary impacts (Figs. 13 and 14c). For instance, the extensive high-reflectance rays emanating from Hokusai crater indicate deposition of excavated crater materials within the NSP. Similar density trends were observed surrounding Orientale basin on the Moon in a study of global crater density by Head et al. (2010). In some cases, such as the areas surrounding craters Abedin, Hokusai, Rustaveli, and Oskison, the irregular boundaries between the areas of low and moderate density reflect both the geological effects of ejecta emplacement and smoothing inherent in the density technique. For each calculation of areal density within one neighborhood area at a particular output cell position, all craters contained within the neighborhood are considered. Thus, the lowest density values occur within the interiors of large impact craters. As the output cell position moves outward relative to a crater interior, the density increases, provided the surrounding region is of higher density, and the density reaches moderate values.

For all but one high-density region in the NSP, variations in the areal density of craters likely reflect the randomness of the cratering process (e.g., Figs. 13, 14a, b, and 15). The single exception for high crater density results from the probable inclusion of circular, non-overlapping secondaries from Strindberg crater (53.21°N, 223.44°E). Smaller, isolated high-density patches (e.g., 72.00°N,

120.00°E) and the scatter of high-density output cells such as those surrounding large high-density regions (e.g., H1 in Fig. 13) may reflect statistical variations in the areal density measurement expected for a random population on the basis of the synthetic density maps.

The extensive areas of moderate crater density across the NSP, coupled with the attribution of low-density regions to impact-related modification of the preexisting surface and of high-density regions to statistical fluctuations, are consistent with a final major volcanic resurfacing event that was restricted to a relatively short interval of geological time. Moreover, the measured crater density reflects a randomly distributed crater population, without clear boundaries between subunits, as demonstrated by comparison with synthetic areal density maps determined from random point distributions. These results imply that earlier episodes of volcanic emplacement were limited in extent. Furthermore, these results suggest that the most recent (and probably last) episode of large-scale volcanic resurfacing within the NSP encompassed nearly the entire region, an interpretation consistent with morphological observations (Section 4.4.1). This explanation is also consistent with the homogeneous MDIS color observations, the presence of Archimedes-like partially flooded craters, the absence of resurfacing kinks in the cumulative SFD for both the post-plains and buried crater populations, and the findings from earlier studies (e.g., Head et al., 2011; Freed et al., 2012; Klimczak et al., 2012).

5. Conclusions

MESSENGER MDIS orbital image data provide the first complete view of Mercury's north polar region at illumination geometries favorable for morphological and crater density studies. Although the Mariner 10 and MESSENGER flybys imaged the full extent of the NSP, the illumination for similar observations of morphology was not optimal until orbital data from MESSENGER were acquired. The northern smooth plains constitute ~7% of the surface area of Mercury and are one of two major largest occurrences of smooth plains on Mercury. The two units of smooth plains identified in the north polar region, NSP1 and NSP2, comprise 5% and 2% of the surface area of Mercury, respectively. No conclusive volcanic landforms are identified within the NSP, but morphological and structural evidence is consistent with a volcanic origin for the plains. For instance, the presence of flow-modified channels closely associated with vent-like features in areas near the NSP (Head et al., 2011; Byrne et al., 2013) and extensional tectonic features hosted by volcanically filled impact craters and basins (Freed et al., 2012; Klimczak et al., 2012; Watters et al., 2012) supports the hypothesis that the NSP were formed rapidly by large volumes of high-temperature, low-viscosity lava, a conclusion also consistent with the high-volume, high-effusion style of volcanism predicted for Mercury (Wilson and Head, 2008, 2012). From buried crater rim height estimates, a conservative volume of the NSP is between 4×10^6 km^3 and 10^7 km^3.

The size–frequency distribution of post-plains craters on the NSP is spatially uniform, to within statistical uncertainty. From its observed post-plains crater population, we infer that the NSP formed by the voluminous outpouring of volcanic material over a short interval of geologic time. In particular, the areal density of impact craters is indistinguishable from a random population, implying that the last resurfacing encompassed the full current extent of the NSP. Stratigraphic relations among buried craters show that at least two periods of volcanic modification occurred prior to the formation of the post-plains crater population. The absence of kinks characteristic of volcanic resurfacing in the cumulative SFDs for the post-plains and buried crater populations suggest that the distinct episodes of volcanic emplacement were separated by one or more geologically brief intervals. Model ages for subsets of buried craters ($D > 30$ km, $D < 30$ km) suggest intervals of 100 My or less. The three current models for absolute crater retention age yield ages for the NSP spanning 1.2 Ga (~3.7–2.5 Ga); i.e., the differences between models far exceed the formal errors in each model, so the uncertainties in such age estimates are dominated by systematic uncertainties in the crater production function. Even so, current estimates for the cratering rate of Mercury indicate that the NSP and other volcanic plains units were emplaced more or less contemporaneously with the primary episode of mare formation on the Moon.

Subunits within the NSP were not detected with MDIS multispectral observations, and coupled with the crater size–frequency distributions, these observations together suggest that the composition of extruded lava did not change markedly over the formation time of the surface on which the post-plains crater population formed. MESSENGER X-Ray Spectrometer (XRS) measurements of the NSP show that the Al/Si, Ca/Si, and Mg/Si ratios are most consistent with a magnesian basalt (Nittler et al., 2011; Stockstill-Cahill et al., 2012; Weider et al., 2012), although there are variations in these ratios across the NSP that are not correlated with unit boundaries mapped on the basis of morphology or color (Weider et al., 2014).

Relative crater size–frequency distributions for the NHCT are consistent with those for average heavily cratered terrain on Mercury, with some variation in crater density observed because crater SFDs on Mercury are highly sensitive to resurfacing and secondary cratering. This variation is consistent with widespread, complex resurfacing that likely resulted from the emplacement of a combination of volcanic and impact-related material during the Late Heavy Bombardment (e.g., Murray, 1975; Strom et al., 1975b; Trask and Guest, 1975; Malin, 1976; Strom, 1977; Whitten et al., 2012, 2014; Denevi et al., 2013b).

The comprehensive cratering history of Mercury's north polar region may now be put into context with other smooth plains on Mercury. On the basis of measured crater density, two extensive regions of smooth plains units in the north polar region are comparable in age to the Caloris interior and exterior smooth plains as well as the Rudaki plains, smooth plains south of Rachmaninoff, and those within Beethoven and Rembrandt basins (Denevi et al., 2013a). The emplacement history of these other regions of smooth plains, however, has not yet been investigated in detail. An examination of the buried crater populations in those areas would improve our understanding of the history of resurfacing for these regions of smooth plains and provide further constraints to the volcanic history of Mercury.

Acknowledgments

We thank the NASA MESSENGER project and science team. We thank Paul Byrne, Brett Denevi, Christian Klimczak, and Rhiannon Weaver for helpful discussions and suggestions regarding earlier versions of this manuscript. We are grateful for constructive reviews by Nadine Barlow and an anonymous reviewer. The MESSENGER project is supported by the NASA Discovery Program under contracts NASW-00002 to the Carnegie Institution of Washington and NAS5-97271 to The Johns Hopkins Applied Physics Laboratory. This work was supported in part by an appointment to the NASA Postdoctoral Program at NASA Goddard Space Flight Center, administered by Oak Ridge Associated Universities through a contract with NASA. This research made use of NASA's Astrophysics Data System.

Appendix A. Crater statistics for NHCT and NSP (post-plains, buried) crater populations

Table A1
N(20) values for craters in NHCT subregions.

Subarea name	Measurement area (km^2)	*N*(10)	*N*(20)
He1a1[a]	1.19×10^6	230 ± 14	111 ± 10
He1a2	1.46×10^6	241 ± 13	101 ± 8
He1a3	1.02×10^6	240 ± 15	108 ± 10
He2a1	1.45×10^6	253 ± 13	122 ± 9
He2a2	1.31×10^6	256 ± 14	111 ± 9
He2a3	9.11×10^5	184 ± 14	74 ± 9
He3a1	1.03×10^6	273 ± 16	120 ± 11
He3a2	1.19×10^6	248 ± 14	119 ± 10
He3a3	1.45×10^6	203 ± 12	86 ± 8

[a] He1a1 = NHCT, example 1, area 1, etc.

Table A2
N(10) values for post-plains craters in NSP1 subregions.

Subarea name	Measurement area (km^2)	*N*(10)[a]	*N*(20)
Ne1a1[b]	1.06×10^6	81 ± 9	30 ± 5
Ne1a2	8.85×10^5	64 ± 9	27 ± 5
Ne1a3	1.08×10^6	69 ± 8	20 ± 4
Ne1a4	1.06×10^6	57 ± 7	19 ± 4
Ne2a1	1.38×10^6	70 ± 7	25 ± 4
Ne2a2	1.14×10^6	78 ± 8	31 ± 5
Ne2a3	7.89×10^5	68 ± 9	20 ± 5
Ne2a4	7.51×10^5	51 ± 8	16 ± 5
Ne3a1	9.61×10^5	69 ± 8	20 ± 4
Ne3a2	1.09×10^6	60 ± 7	18 ± 4
Ne3a3	1.27×10^6	75 ± 8	31 ± 5
Ne3a4	7.58×10^5	69 ± 10	26 ± 6

[a] *N*(10) = 67 ± 4 for NSP1.
[b] Ne1a1 = NSP1, example 1, area 1, etc.

Table A3
NHCT crater population data.

Diameter (km)[a]	Area (km^2)	Cumulative			R plot		
		N_{cum}[b]	Frequency	Uncertainty[c]	n[d]	Relative value	Uncertainty[c]
8	3.67×10^6	1056	2.88×10^{-4}	1.64×10^{-5}	306	0.021666	1.24×10^{-3}
11.31	3.67×10^6	750	2.04×10^{-4}	1.27×10^{-5}	258	0.036535	2.27×10^{-3}
16	3.67×10^6	492	1.34×10^{-4}	1.07×10^{-5}	156	0.044182	3.54×10^{-3}
22.63	3.67×10^6	336	9.16×10^{-5}	8.89×10^{-6}	106	0.060042	5.83×10^{-3}
32	3.67×10^6	230	6.27×10^{-5}	6.21×10^{-6}	102	0.115553	1.14×10^{-2}
45.25	3.67×10^6	128	3.49×10^{-5}	4.54×10^{-6}	59	0.133679	1.74×10^{-2}
64	3.67×10^6	69	1.88×10^{-5}	2.90×10^{-6}	42	0.190323	2.94×10^{-2}
90.51	3.67×10^6	27	7.36×10^{-6}	1.97×10^{-6}	14	0.126882	3.39×10^{-2}
128	3.67×10^6	13	3.54×10^{-6}	1.18×10^{-6}	9	0.163134	5.44×10^{-2}
181	3.67×10^6	4	1.09×10^{-6}	6.29×10^{-6}	3	0.108756	6.28×10^{-2}
256	3.67×10^6	1	2.72×10^{-7}	2.72×10^{-7}	1	0.072504	7.25×10^{-2}

[a] Diameter (km) for lower bin limit.
[b] Cumulative number of craters per diameter bin.
[c] Uncertainties equal the square root of the number of craters for a given bin.
[d] Number of craters per diameter bin.

Table A4
NSP post-plains crater population data.

Diameter (km)[a]	Area (km^2)	Cumulative			R plot		
		N_{cum}[b]	Frequency	Uncertainty[c]	n[d]	Relative value	Uncertainty[c]
8	5.59×10^6	501	8.96×10^{-5}	6.17×10^{-6}	211	0.009808	6.75×10^{-4}
11.31	5.59×10^6	290	5.19×10^{-5}	4.95×10^{-6}	110	0.010227	9.75×10^{-4}
16	5.59×10^6	180	3.22×10^{-5}	3.49×10^{-6}	85	0.015805	1.71×10^{-3}
22.63	5.59×10^6	95	1.70×10^{-5}	2.43×10^{-6}	49	0.018222	2.60×10^{-3}
32	5.59×10^6	46	8.23×10^{-6}	1.68×10^{-6}	24	0.017850	3.64×10^{-3}
45.25	5.59×10^6	22	3.94×10^{-6}	1.24×10^{-6}	10	0.014875	4.70×10^{-3}
64	5.59×10^6	12	2.15×10^{-6}	8.76×10^{-7}	6	0.017850	7.29×10^{-3}
90.51	5.59×10^6	6	1.07×10^{-6}	4.80×10^{-7}	5	0.029751	1.33×10^{-2}
128	5.59×10^6	1	1.79×10^{-7}	1.79×10^{-7}	0	0	0
181	5.59×10^6	1	1.79×10^{-7}	1.79×10^{-7}	1	0.023801	2.38×10^{-2}

[a] Diameter (km) for lower bin limit.
[b] Cumulative number of craters per diameter bin.
[c] Uncertainties equal the square root of the number of craters for a given bin.
[d] Number of craters per diameter bin.

Table A5
NSP buried crater population data.

Diameter (km)[a]	Area (km^2)	Cumulative			R plot		
		N_{cum}[b]	Frequency	Uncertainty[c]	n[d]	Relative value	Uncertainty[c]
8	3.79×10^6	355	9.37×10^{-5}	9.66×10^{-6}	94	0.007110	6.65×10^{-4}
11.31	3.79×10^6	261	6.89×10^{-5}	8.41×10^{-6}	67	0.010310	1.12×10^{-3}
16	3.79×10^6	194	5.12×10^{-5}	7.17×10^{-6}	51	0.015945	1.96×10^{-3}
22.63	3.79×10^6	143	3.77×10^{-5}	5.97×10^{-6}	40	0.025409	3.47×10^{-3}
32	3.79×10^6	103	2.72×10^{-5}	5.05×10^{-6}	59	0.073150	8.43×10^{-3}
45.25	3.79×10^6	74	1.95×10^{-5}	3.40×10^{-6}	33	0.085006	1.26×10^{-2}
64	3.79×10^6	41	1.08×10^{-5}	2.36×10^{-6}	21	0.112257	2.01×10^{-2}
90.51	3.79×10^6	20	5.28×10^{-6}	2.64×10^{-6}	4	0.052656	1.76×10^{-2}
128	3.79×10^6	16	4.22×10^{-6}	1.60×10^{-6}	7	0.169303	4.64×10^{-2}
181.02	3.79×10^6	9	2.37×10^{-6}	1.19×10^{-6}	4	0.210625	7.02×10^{-2}
256	3.79×10^6	5	1.32×10^{-6}	9.33×10^{-7}	2	0.239706	9.93×10^{-2}
362.04	3.79×10^6	3	7.92×10^{-7}	5.60×10^{-7}	2	0.479413	1.99×10^{-1}

[a] Diameter (km) for lower bin limit.
[b] Cumulative number of craters per diameter bin.
[c] Uncertainties equal the square root of the number of craters for a given bin.
[d] Number of craters per diameter bin.

References

Arthur, D.W.G. et al., 1964. No. 30. The system of lunar craters, quadrant I. Comm. Lunar Planet. Lab. 2, 71–78.

Baker, D.M.H. et al., 2011. The transition from complex crater to peak-ring basin on Mercury: New observations from MESSENGER flyby data and constraints on basin formation models. Planet. Space Sci. 59, 1932–1948. http://dx.doi.org/10.1016/j.pss.2011.05.010.

Barnouin, O.S. et al., 2012. The morphology of craters on Mercury: Results from MESSENGER flybys. Icarus 219, 414–427. http://dx.doi.org/10.1016/j.icarus.2012.02.029.

Bugiolacchi, R., Guest, J.E., 2008. Compositional and temporal investigation of exposed lunar basalts in the Mare Imbrium region. Icarus 197, 1–18. http://dx.doi.org/10.1016/j.icarus.2008.04.001.

Byrne, P.K. et al., 2013. An assemblage of lava flow features on Mercury. J. Geophys. Res. Planets 118, 1303–1322. http://dx.doi.org/10.1002/jgre.20052.

Coffin, M.F., Eldholm, O., 1994. Large igneous provinces: Crustal structure, dimensions, and external consequences. Rev. Geophys. 32, 1–36. http://dx.doi.org/10.1029/93RG02508.

Crater Analysis Techniques Working Group, 1979. Standard techniques for presentation and analysis of crater size–frequency data. Icarus 37, 467–474. http://dx.doi.org/10.1016/0019-1035(79)90009-5.

Danielson, G.E., Klaasen, K.P., Anderson, J.L., 1975. Acquisition and description of Mariner 10 television science data at Mercury. J. Geophys. Res. 80, 2357–2393. http://dx.doi.org/10.1029/JB080i017p02357.

Davis, J.C., 2002. Statistics and Data Analysis in Geology, third ed. John Wiley & Sons, New York, 638 pp.

De Hon, R.A., 1974. Thickness of mare material in the Tranquillitatis and Nectaris basins. Proc. Lunar Sci. Conf. 5, 53–59.

Denevi, B.W. et al., 2009. The evolution of Mercury's crust: A global perspective from MESSENGER. Science 324, 613–618. http://dx.doi.org/10.1126/science.1172226.

Denevi, B.W. et al., 2013a. The distribution and origin of smooth plains on Mercury. J. Geophys. Res. Planets 118, 891–907. http://dx.doi.org/10.1002/jgre.20075.

Denevi, B.W. et al., 2013b. The volcanic origin of a region of intercrater plains on Mercury. Lunar Planet. Sci. 44. Abstract 1218.

Domingue, D.L. et al., 2013. MESSENGER's Mercury global color mosaic: Photometric update. Lunar Planet. Sci. 44. Abstract 1324.

Ernst, C.M. et al., 2010. Exposure of spectrally distinct material by impact craters on Mercury: Implications for global stratigraphy. Icarus 209, 210–223. http://dx.doi.org/10.1016/j.icarus.2010.05.022.

Fassett, C.I. et al., 2009. Caloris impact basin: Exterior geomorphology, stratigraphy, morphometry, radial sculpture, and smooth plains deposits. Earth Planet. Sci. Lett. 285, 297–308. http://dx.doi.org/10.1016/j.epsl.2009.05.022.

Fassett, C.I. et al., 2011. The global population of large craters on Mercury and comparison with the Moon. Geophys. Res. Lett. 38, L10202. http://dx.doi.org/10.1029/2011GL047294.

Fassett, C.I. et al., 2012. Large impact basins on Mercury: Global distribution, characteristics, and modification history from MESSENGER orbital data. J. Geophys. Res. 117, E00L08. http://dx.doi.org/10.1029/2012JE004154.

Freed, A.M. et al., 2012. On the origin of graben and ridges within and near volcanically buried craters and basins in Mercury's northern plains. J. Geophys. Res. 117, E00L06. http://dx.doi.org/10.1029/2012JE004119.

Gault, D.E. et al., 1975. Some comparisons of impact craters on Mercury and the Moon. J. Geophys. Res. 80, 2444–2460. http://dx.doi.org/10.1029/JB080i017p02444.

Gault, D.E. et al., 1977. Mercury. Annu. Rev. Astron. Astrophys. 15, 97–126. http://dx.doi.org/10.1146/annurev.aa.15.090177.000525.

Goudge, T.A. et al., 2014. Global inventory and characterization of pyroclastic deposits on Mercury: New insights into pyroclastic activity from MESSENGER orbital data. J. Geophys. Res. Planets 119, 635–658. http://dx.doi.org/10.1002/2013JE004480.

Grolier, M.J., Boyce, J.M., 1984. Geologic map of the Borealis Region (H-1) of Mercury. Map I-1660, Misc. Investigations Ser., U.S. Geological Survey, Denver, Colo.

Guest, J.E., Gault, D.E., 1976. Crater populations in the early history of Mercury. Geophys. Res. Lett. 3, 121–123. http://dx.doi.org/10.1029/GL003i003p00121.

Hawkins III, S.E. et al., 2007. The Mercury Dual Imaging System on the MESSENGER spacecraft. Space Sci. Rev. 131, 247–338. http://dx.doi.org/10.1007/s11214-007-9266-3.

Head, J.W., 1982. Lava flooding of ancient planetary crusts: Geometry, thickness, and volumes of flooded lunar impact basins. Moon Planets 26, 61–88. http://dx.doi.org/10.1007/BF00941369.

Head III, J.W., Wilson, L., 1992. Lunar mare volcanism: Stratigraphy, eruption conditions, and the evolution of secondary crusts. Geochim. Cosmochim. Acta 56, 2155–2175. http://dx.doi.org/10.1016/0016-7037(92)90183-J.

Head III, J.W., Kreslavsky, M.A., Pratt, S., 2002. Northern lowlands of Mars: Evidence for widespread volcanic flooding and tectonic deformation in the Hesperian Period. J. Geophys. Res. 107 (E1), 5003. http://dx.doi.org/10.1029/2000JE001445.

Head, J.W. et al., 2008. Volcanism on Mercury: Evidence from the first MESSENGER flyby. Science 321, 69–72. http://dx.doi.org/10.1126/science.1159256.

Head, J.W. et al., 2009a. Volcanism on Mercury: Evidence from the first MESSENGER flyby for extrusive and explosive activity and the volcanic origin of plains. Earth Planet. Sci. Lett. 285, 227–242. http://dx.doi.org/10.1016/j.epsl.2009.03.007.

Head, J.W. et al., 2009b. Evidence for intrusive activity on Mercury from the first MESSENGER flyby. Earth Planet. Sci. Lett. 285, 251–262. http://dx.doi.org/10.1016/j.epsl.2009.03.008.

Head, J.W. et al., 2010. Global distribution of large lunar craters: Implications for resurfacing and impactor populations. Science 329, 1504–1507. http://dx.doi.org/10.1126/science.1195050.

Head, J.W. et al., 2011. Flood volcanism in the northern high latitudes of Mercury revealed by MESSENGER. Science 333, 1853–1856. http://dx.doi.org/10.1126/science.1211997.

Hiesinger, H. et al., 2000. Ages of mare basalts on the lunar nearside. J. Geophys. Res. 105, 29239–29275. http://dx.doi.org/10.1029/2000JE001244.

Hiesinger, H. et al., 2002. Lunar mare basalt flow units: Thicknesses determined from crater size–frequency distributions. Geophys. Res. Lett. 29 (8), 1248. http://dx.doi.org/10.1029/2002GL014847.

Hurwitz, D.M. et al., 2013. Investigating the origin of candidate lava channels on Mercury with MESSENGER data: Theory and observations. J. Geophys. Res. Planets 118, 471–486. http://dx.doi.org/10.1029/2012JE004103.

Keller, M.R. et al., 2013. Time-dependent calibration of MESSENGER's wide-angle camera following a contamination event. Lunar Planet. Sci. 44. Abstract 2489.

Kerber, L.A. et al., 2009. Explosive volcanic eruptions on Mercury: Eruption conditions, magma volatile content, and implications for interior volatile abundances. Earth Planet. Sci. Lett. 285, 263–271. http://dx.doi.org/10.1016/j.epsl.2009.04.037.

Kerber, L.A. et al., 2011. The global distribution of pyroclastic deposits on Mercury: The view from MESSENGER flybys 1–3. Planet. Space Sci. 59, 1895–1909. http://dx.doi.org/10.1016/j.pss.2011.03.020.

Kiefer, W.S., Murray, B.C., 1987. The formation of Mercury's smooth plains. Icarus 72, 477–491. http://dx.doi.org/10.1016/0019-1035(87)90046-7.

Klimczak, C. et al., 2012. Deformation associated with ghost craters and basins in volcanic smooth plains on Mercury: Strain analysis and implications for plains evolution. J. Geophys. Res. 117, E00L03. http://dx.doi.org/10.1029/2012JE004100.
Kneissl, T., van Gasselt, S., Neukum, G., 2011. Map-projection-independent crater size–frequency determination in GIS environments—New software tool for ArcGIS. Planet. Space Sci. 59, 1243–1254. http://dx.doi.org/10.1016/j.pss.2010.03.015.
Le Feuvre, M., Wieczorek, M.A., 2011. Nonuniform cratering of the Moon and a revised crater chronology of the inner Solar System. Icarus 214, 1–20. http://dx.doi.org/10.1016/j.icarus.2011.03.010.
Leake, M.A., 1982. The intercrater plains of Mercury and the Moon: Their nature, origin, and role in terrestrial planet evolution. In: Advances in Planetary Geology, Technical Memorandum 84894. NASA, Washington, DC, pp. 1–537.
Malin, M.C., 1976. Observations of intercrater plains on Mercury. Geophys. Res. Lett. 3, 581–584. http://dx.doi.org/10.1029/GL003i010p00581.
Malin, M.C., 1978. Surfaces of Mercury and the Moon: Effects of resolution and lighting conditions on the discrimination of volcanic features. Proc. Lunar Planet. Sci. Conf. 9, 3395–3409.
Marchi, S., Morbidelli, A., Cremonese, G., 2005. Flux of meteoroid impacts on Mercury. Astron. Astrophys. 431, 1123–1127. http://dx.doi.org/10.1051/0004-6361:20041800.
Marchi, S. et al., 2009. A new chronology for the Moon and Mercury. Astron. J. 137, 4936–4948. http://dx.doi.org/10.1088/0004-6256/137/6/4936.
Marchi, S. et al., 2011. The effects of the target material properties and layering on the crater chronology: The case of Raditladi and Rachmaninoff basins on Mercury. Planet. Space Sci. 59, 1968–1980. http://dx.doi.org/10.1016/j.pss.2011.06.007.
Marchi, S. et al., 2013. Global resurfacing of Mercury 4.0–4.1 billion years ago by heavy bombardment and volcanism. Nature 499, 59–61. http://dx.doi.org/10.1038/nature12280.
McGill, G.E., 1977. Craters as "fossils": The remote dating of planetary surface materials. Geol. Soc. Am. Bull. 88, 1102–1110. http://dx.doi.org/10.1130/0016-7606(1977)88<1102:CAFTRD>2.0.CO;2.
Michael, G.G., Neukum, G., 2010. Planetary surface dating from crater size–frequency distribution measurements: Partial resurfacing events and statistical age uncertainty. Earth Planet. Sci. Lett. 294, 223–229. http://dx.doi.org/10.1016/j.epsl.2009.12.041.
Milkovich, S.M., Head, J.W., Wilson, L., 2002. Identification of mercurian volcanism: Resolution effects and implications for MESSENGER. Meteorit. Planet. Sci. 37, 1209–1222. http://dx.doi.org/10.1111/j.1945-5100.2002.tb00890.x.
Murchie, S.L. et al., 2008. Geology of the Caloris basin, Mercury: A view from MESSENGER. Science 321, 73–76. http://dx.doi.org/10.1126/science.1159261.
Murray, B.C., 1975. The Mariner 10 pictures of Mercury: An overview. J. Geophys. Res. 80, 2342–2344. http://dx.doi.org/10.1029/JB080i017p02342.
Murray, B.C. et al., 1974a. Mariner 10 pictures of Mercury: First results. Science 184, 459–461. http://dx.doi.org/10.1126/science.184.4135.459.
Murray, B.C. et al., 1974b. Mercury's surface: Preliminary description and interpretation from Mariner 10 pictures. Science 185, 169–179. http://dx.doi.org/10.1126/science.185.4146.169.
Neukum, G., 1983. Meteorite Bombardment and Dating of Planetary Surfaces. Dissertation on Attaining Venia Legendi (Tenure) in the Geophysics Department in the Faculty of Geological Sciences of the Ludwig-Maximilians University, Munich, West Germany. 186 pp. (translated from German).
Neukum, G., Horn, P., 1976. Effects of lava flows on lunar crater populations. Moon 15, 205–222. http://dx.doi.org/10.1007/BF00562238.
Neukum, G., Ivanov, B.A., Hartmann, W.K., 2001a. Cratering records in the inner Solar System in relation to the lunar reference system. Space Sci. Rev. 96, 55–86. http://dx.doi.org/10.1023/A:1011989004263.
Neukum, G. et al., 2001b. Geologic evolution and cratering history of Mercury. Planet. Space Sci. 49, 1507–1521. http://dx.doi.org/10.1016/S0032-0633(01)00089-7.
Neukum, G. et al., 2010. The geologic evolution of Mars: Episodicity of resurfacing events and ages from cratering analysis of image data and correlation with radiometric ages of martian meteorites. Earth Planet. Sci. Lett. 294, 204–222. http://dx.doi.org/10.1016/j.epsl.2009.09.006.
Nittler, L.R. et al., 2011. The major-element composition of Mercury's surface from MESSENGER X-ray spectrometry. Science 333, 1847–1850. http://dx.doi.org/10.1126/science.1211567.
Oberbeck, V.R. et al., 1977. Comparative studies of lunar, martian, and mercurian craters and plains. J. Geophys. Res. 82, 1681–1698. http://dx.doi.org/10.1029/JB082i011p01681.
Ostrach, L.R., Robinson, M.S., 2014. Areal crater density analysis of volcanic smooth plains: Mare Imbrium, a revised approach. Lunar Planet. Sci. 45. Abstract 1266.
Pike, R.J., 1988. Geomorphology of impact craters on Mercury. In: Vilas, F., Chapman, C.R., Matthews, M.S. (Eds.), Mercury. University of Arizona Press, Tucson, Ariz., pp. 165–273.
Prockter, L.M. et al., 2010. Evidence for young volcanism on Mercury from the third MESSENGER flyby. Science 329, 668–671. http://dx.doi.org/10.1126/science.1188186.
Robinson, M.S., Lucey, P.G., 1997. Recalibrated Mariner 10 color mosaics: Implications for mercurian volcanism. Science 275, 197–200. http://dx.doi.org/10.1126/science.275.5297.197.
Robinson, M.S., Taylor, G.J., 2001. Ferrous oxide in Mercury's crust and mantle. Meteorit. Planet. Sci. 36, 841–847. http://dx.doi.org/10.1111/j.1945-5100.2001.tb01921.x.
Robinson, M.S. et al., 1999. A revised control network for Mercury. J. Geophys. Res. 104, 30847–30852. http://dx.doi.org/10.1029/1999JE001081.
Robinson, M.S. et al., 2008. Reflectance and color variations on Mercury: Regolith processes and compositional heterogeneity. Science 321, 66–69. http://dx.doi.org/10.1126/science.1160080.
Schultz, P.H., 1977. Endogenic modification of impact craters on Mercury. Phys. Earth Planet. Inter. 15, 202–219. http://dx.doi.org/10.1016/0031-9201(77)90032-2.
Silverman, B.W., 1986. Density Estimation for Statistics and Data Analysis. Chapman and Hall, New York, 176 pp.
Solomon, S.C. et al., 2001. The MESSENGER mission to Mercury: Scientific objectives and implementation. Planet. Space Sci. 49, 1445–1465. http://dx.doi.org/10.1016/S0032-0633(01)00085-X.
Solomon, S.C. et al., 2008. Return to Mercury: A global perspective on MESSENGER's first Mercury flyby. Science 321, 59–62. http://dx.doi.org/10.1126/science.1159706.
Spudis, P.D., Guest, J.E., 1988. Stratigraphy and geologic history of Mercury. In: Vilas, F., Chapman, C.R., Matthews, M.S. (Eds.), Mercury. University of Arizona Press, Tucson, Ariz., pp. 118–164.
Stockstill-Cahill, K.R. et al., 2012. Magnesium-rich crustal compositions on Mercury: Implications for magmatism from petrologic modeling. J. Geophys. Res. 117, E00L15. http://dx.doi.org/10.1029/2012JE004140.
Strom, R.G., 1977. Origin and relative age of lunar and mercurian intercrater plains. Phys. Earth Planet. Inter. 15, 156–172. http://dx.doi.org/10.1016/0031-9201(77)90028-0.
Strom, R.G., Neukum, G., 1988. The cratering record on Mercury and the origin of impacting objects. In: Vilas, F., Chapman, C.R., Matthews, M.S. (Eds.), Mercury. University of Arizona Press, Tucson, Ariz., pp. 336–373.
Strom, R.G. et al., 1975a. Preliminary imaging results from the second Mercury encounter. J. Geophys. Res. 80, 2345–2356. http://dx.doi.org/10.1029/JB080i017p02345.
Strom, R.G., Trask, N.J., Guest, J.E., 1975b. Tectonism and volcanism on Mercury. J. Geophys. Res. 80, 2478–2507. http://dx.doi.org/10.1029/JB080i017p02478.
Strom, R.G. et al., 2005. The origin of planetary impactors in the inner Solar System. Science 309, 1847–1850. http://dx.doi.org/10.1126/science.1113544.
Strom, R.G. et al., 2008. Mercury cratering record viewed from MESSENGER's first flyby. Science 321, 79–81. http://dx.doi.org/10.1126/science.1159317.
Strom, R.G. et al., 2011. Mercury crater statistics from MESSENGER flybys: Implications for stratigraphy and resurfacing history. Planet. Space Sci. 59, 1960–1967. http://dx.doi.org/10.1016/j.pss.2011.03.018.
Trask, N.J., 1975. Cratering history of the heavily cratered terrain on Mercury. Geol. Romana 15, 471–476.
Trask, N.J., Guest, J.E., 1975. Preliminary geologic terrain map of Mercury. J. Geophys. Res. 80, 2461–2477. http://dx.doi.org/10.1029/JB080i017p02461.
Trask, N.J., Strom, R.G., 1976. Additional evidence of mercurian volcanism. Icarus 28, 559–563. http://dx.doi.org/10.1016/0019-1035(76)90129-9.
Watters, T.R., 1993. Compressional tectonism on Mars. J. Geophys. Res. 98, 17049–17060. http://dx.doi.org/10.1029/93JE01138.
Watters, T.R. et al., 2009. Emplacement and tectonic deformation of smooth plains in the Caloris basin, Mercury. Earth Planet. Sci. Lett. 285, 309–319. http://dx.doi.org/10.1016/j.epsl.2009.03.040.
Watters, T.R. et al., 2012. Extension and contraction within volcanically buried impact craters and basins on Mercury. Geology 40, 1123–1126. http://dx.doi.org/10.1130/G33725.1.
Weider, S.Z. et al., 2012. Chemical heterogeneity on Mercury's surface revealed by the MESSENGER X-Ray Spectrometer. J. Geophys. Res. 117, E00L05. http://dx.doi.org/10.1029/2012JE004153.
Weider, S.Z. et al., 2014. Geochemical terranes on the innermost planet: Possible origins of Mercury's high-magnesium region. Lunar Planet. Sci. 45. Abstract 1866.
Whitten, J.L. et al., 2012. Intercrater plains on Mercury: Topographic assessment with MESSENGER data. Lunar Planet. Sci. 43. Abstract 1479.
Whitten, J.L. et al., 2014. Intercrater plains on Mercury: Insights into unit definition, characterization, and origin from MESSENGER datasets. Icarus 241, 97–113.
Wilhelms, D.E., 1976. Mercurian volcanism questioned. Icarus 28, 551–558. http://dx.doi.org/10.1016/0019-1035(76)90128-7.
Wilhelms, D.E., 1987. The geologic history of the Moon. Professional Paper 1348. U.S. Geological Survey, Denver, Colo., 302 pp.
Wilhelms, D.E., McCauley, J.F., 1971. Geologic map of the near side of the Moon. Map I-703, Misc. Investigations Ser., U.S. Geological Survey, Denver, Colo.
Williams, K.K., Zuber, M.T., 1998. Measurement and analysis of lunar basin depths from Clementine altimetry. Icarus 131, 107–122. http://dx.doi.org/10.1006/icar.1997.5856.
Williams, D.A. et al., 2008. Tyrrhena Patera: Geologic history derived from *Mars Express* High Resolution Stereo Camera. J. Geophys. Res. 113, E11005. http://dx.doi.org/10.1029/2008JE003104.
Wilson, L., Head, J.W., 2008. Volcanism on Mercury: A new model for the history of magma ascent and eruption. Geophys. Res. Lett. 35, L23205. http://dx.doi.org/10.1029/2008GL035620.
Wilson, L., Head, J.W., 2012. Volcanic eruption processes on Mercury. Lunar Planet. Sci. 43. Abstract 1316.
Zuber, M.T. et al., 2012. Topography of the northern hemisphere of Mercury from MESSENGER laser altimetry. Science 336, 217–220. http://dx.doi.org/10.1126/science.1218805.